

Space Robots

45. Space Robots and Systems

Kazuya Yoshida, Brian Wilcox

In the space community, any unmanned spacecraft can be called a robotic spacecraft. However, *space robots* are considered to be more capable devices that can facilitate manipulation, assembling, or servicing functions in orbit as assistants to astronauts, or to extend the areas and abilities of exploration on remote planets as surrogates for human explorers.

In this chapter, a concise digest of the historical overview and technical advances of two distinct types of space robotic systems, orbital robots and surface robots, is provided. In particular, Sect. 45.1 describes orbital robots, and Sect. 45.2 describes surface robots. In Sect. 45.3, the mathematical modeling of the dynamics and control using reference equations are discussed. Finally, advanced topics for future space exploration missions are addressed in Sect. 45.4.

Key issues in space robots and systems are characterized as follows. *Manipulation* – Although manipulation is a basic technology in robotics, microgravity in the orbital environment requires special attention to the motion dynamics of manipulator arms and objects being handled. Reaction dynamics that affect the base body, impact dynamics when the robotic hand contacts an object to be handled, and vibration dynamics due to structural flexibility are included in this issue. *Mobility* – The ability to locomote is particularly important in exploration robots (rovers) that travel on the surface of a remote planet. These surfaces are natural and rough, and thus challenging to traverse. Sensing and perception, traction mechanics, and vehicle dynamics, control, and navigation are all mobile robotics technologies that must be demonstrated in a natural untouched environment. *Teleoperation and autonomy* – There is a significant time delay between a robotic system at a work site and a human operator in an operation room on the Earth. In earlier orbital robotics demonstrations, the latency was typically 5 s, but

can be several tens of minutes, or even hours for planetary missions. Telerobotics technology is therefore an indispensable ingredient in space robotics, and the introduction of autonomy is a reasonable consequence. *Extreme environments* – In addition to the microgravity environment that affects the manipulator dynamics or the natural and rough terrain that affects surface mobility, there are a number of issues related to extreme space environments that are challenging and must be solved in order to enable practical engineering applications. Such issues include extremely high or low temperatures, high vacuum or high pressure, corrosive atmospheres, ionizing radiation, and very fine dust.

45.1 Historical Developments and Advances of Orbital Robotic Systems	1032
45.1.1 Space Shuttle Remote Manipulator System	1032
45.1.2 ISS-Mounted Manipulator Systems	1033
45.1.3 ROTEX	1035
45.1.4 ETS-VII	1035
45.1.5 Ranger	1036
45.1.6 Orbital Express	1036
45.2 Historical Developments and Advances of Surface Robotic Systems	1037
45.2.1 Teleoperated Rovers	1037
45.2.2 Autonomous Rovers	1039
45.2.3 Research Systems	1042
45.2.4 Sensing and Perception	1043
45.2.5 Estimation	1043
45.2.6 Manipulators for In Situ Science	1044
45.3 Mathematical Modeling	1044
45.3.1 Space Robot as an Articulated-Body System	1044
45.3.2 Equations for Free-Floating Manipulator Systems	1045
45.3.3 Generalized Jacobian and Inertia Matrices	1045
45.3.4 Linear and Angular Momenta	1047
45.3.5 Virtual Manipulator	1047

45.3.6	Dynamic Singularity.....	1047	45.4	Future Directions of Orbital and Surface Robotic Systems.....	1056
45.3.7	Reaction Null Space (RNS)	1048	45.4.1	Robotic Maintenance and Service Missions.....	1056
45.3.8	Equations for Flexible-Based Manipulator Systems	1048	45.4.2	Robonaut.....	1057
45.3.9	Advanced Control for Flexible Structure Based Manipulators	1049	45.4.3	Aerial Platforms	1057
45.3.10	Contact Dynamics and Impedance Control.....	1050	45.4.4	Subsurface Platforms	1059
45.3.11	Dynamics of Mobile Robots.....	1052	45.5	Conclusions and Further Reading.....	1060
45.3.12	Wheel Traction Mechanics	1053	References		1060

45.1 Historical Developments and Advances of Orbital Robotic Systems

The first robotic manipulator arm used in the orbital environment was the Space Shuttle remote manipulator system. It was successfully demonstrated in the STS-2 mission in 1981 and is still operational today. This success opened a new era of orbital robotics and inspired a number of mission concepts to the research community. One ultimate goal that has been discussed intensively after the early 1980s is the application to the rescue and servicing of malfunctioning spacecraft by a robotic free-flyer or free-flying space robot (see, for example, the Space Application of Automation, Robotics and Machine Intelligence (ARAMIS) report [45.1], Fig. 45.1). In later years, manned service missions were conducted for the capture–repair–deploy procedure of malfunctioning satellites (Anik-B, Intelsat 6, for example) and for the maintenance of the Hubble space telescope (STS-61, 82, 103, and 109).

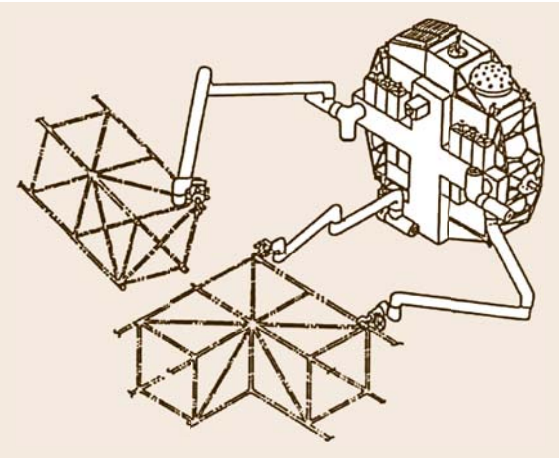


Fig. 45.1 A conceptual design of a telerobotic servicer [45.1]

For all of the above examples, the Space Shuttle, a manned spacecraft with dedicated maneuverability was used. However, unmanned servicing missions have not yet become operational. Although there were several demonstration flights, such as engineering test satellite (ETS)-VII and Orbital Express (to be elaborated later), the practical technologies for unmanned satellite servicing missions await solutions to future challenges.

45.1.1 Space Shuttle Remote Manipulator System

Onboard the Space Shuttle, the *shuttle remote manipulator system (SRMS)*, or Canadarm, is a mechanical arm that maneuvers a payload from the payload bay of the Space Shuttle orbiter to its deployment position and then releases it [45.2]. It can also grapple a free-flying payload and berth it to the payload bay of the orbiter. The SRMS was first used on the second Space Shuttle mission STS-2, launched in 1981. Since then, it has been used more than 100 times during Space Shuttle flight missions, performing such payload deployment or berthing as well as assisting human *extravehicular activities (EVAs)*. Servicing and maintenance missions to the Hubble space telescope and construction tasks of the International Space Station have also been successfully carried out by the cooperative use of the SRMS with human EVAs.

As depicted in Fig. 45.2, the SRMS arm is 15 m long and has six degrees of freedom, comprising shoulder yaw and pitch joints, an elbow pitch joint and wrist pitch, yaw, and roll joints. Attached to the end of the arm is a special gripper system called the *standard end-effector (SEE)*, which is designed to grasp a pole-like fixture (GF) attached to the payload.

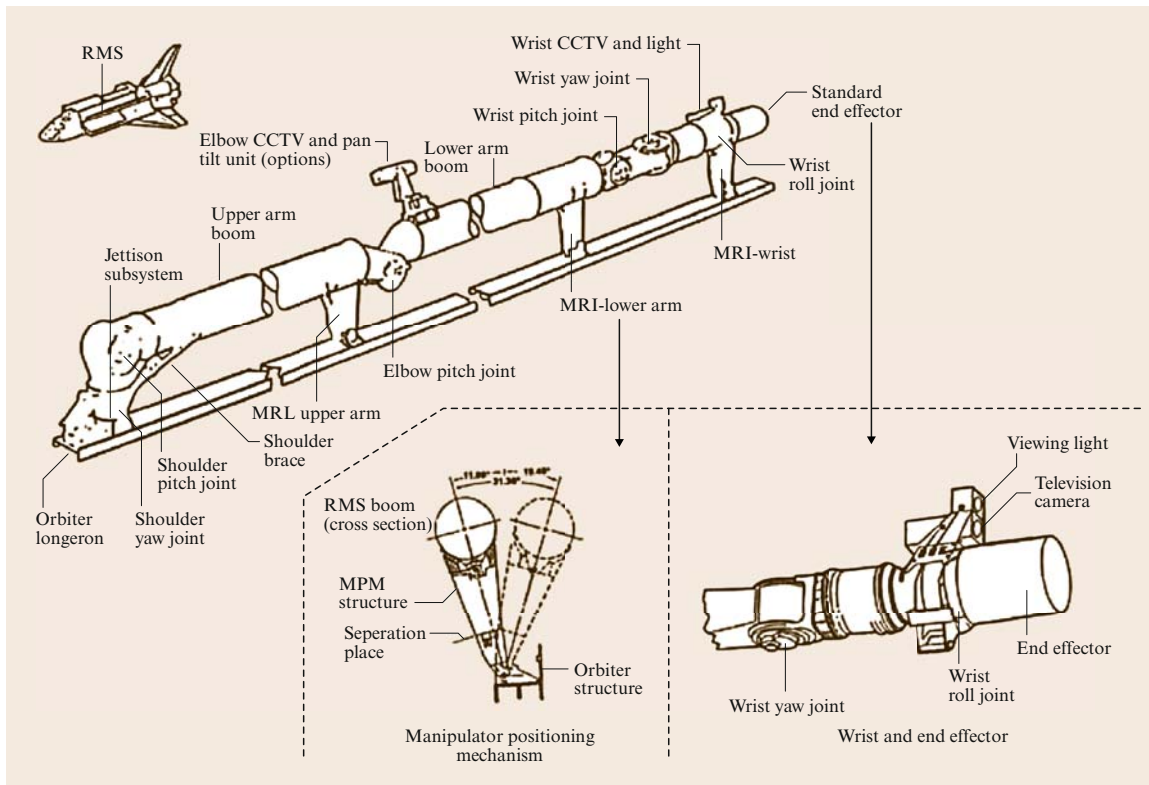


Fig. 45.2 The space shuttle remote manipulator system (SRMS) [45.2]; manipulator retention latch (MRL), manipulator positioning mechanism (MPM), remote manipulator system (RMS)

By attaching a foothold at the end point, the arm can serve as a mobile platform for an astronaut's extravehicular activities (Fig. 45.3).

After the Space Shuttle COLUMBIA accident during STS-107, the National Aeronautics and Space Administration (NASA) outfitted the SRMS with the orbiter boom sensor system (OBSS) – a boom containing instruments to inspect the exterior of the shuttle for damage to the thermal protection system [45.3]. The SRMS is expected to play a role in all future shuttle missions.

45.1.2 ISS-Mounted Manipulator Systems

The International Space Station (ISS) is the largest international technology project, with 15 countries making significant cooperative contributions. The ISS is an *out-post* of the human presence in space, as well as a *flying laboratory* with substantial facilities for science and engineering research. In order to facilitate various activities on the station, there are several robotic systems, some

of which are already operational, while others are ready for launch.

The *space station remote manipulator system* (SSRMS) or Canadarm 2, (Fig. 45.4), is the next generation of the SRMS, for use on the ISS [45.4]. Launched in 2001 during STS-100 (ISS assembly flight 6A), the SSRMS has played a key role in the construction and maintenance of the ISS both by assisting astronauts during EVAs and using the SRMS on the Space Shuttle to hand over a payload from the Space Shuttle to the SSRMS. The arm is 17.6 m long when fully extended and has seven degrees of freedom. Latching end-effectors, through which power, data, and video can be transmitted to and from the arm, are attached to both ends. The SSRMS is self-relocatable using an inch-worm-like movement with alternate grapples of *power data grapple fixtures* (PDGFs), which are installed over the station's exterior surfaces to provide the power, data, and video, as well as a foothold.

As another mobility aid for the SSRMS to cover wider areas of the ISS, a *mobile base system* (MBS) was

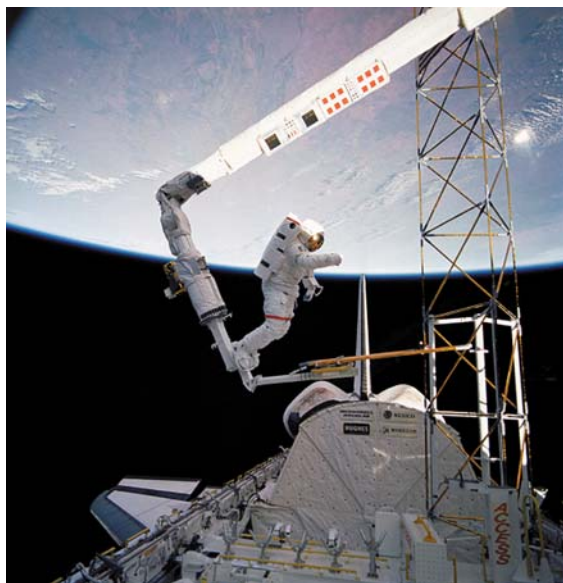


Fig. 45.3 Space shuttle remote manipulator system (SRMS) used as a platform for an astronaut's extravehicular activity in the shuttle cargo bay

added in 2002 by STS-111 (ISS assembly flight UF-2). The MBS provides lateral mobility as it traverses the rails on the main trusses [45.5].

The *special-purpose dexterous manipulator* (SPDM), or Dextre, which will be attached at the end of the SSRM, is a capable mini-arm system to facilitate the delicate assembly tasks currently handled by astronauts

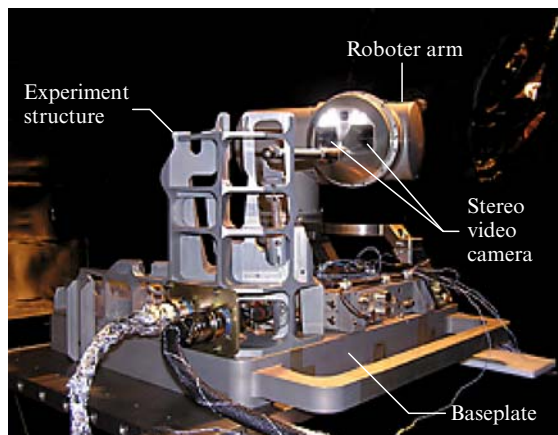


Fig. 45.5 Laboratory test bed for the ROKVISS manipulator system

during EVAs. The SPDM is a dual-arm manipulator system, where each manipulator has seven degrees of freedom and is mounted on a one-degree-of-freedom body joint. Each arm has a special tool mechanism dedicated to the handling of standardized *orbital replacement units* (ORUs). The arms will be teleoperated from a *robotic work station* (RWS) inside the space station [45.6].

The *European Space Agency* (ESA) will also provide a robotic manipulator system for the ISS, the *European robotic arm* (ERA), which be used mainly to work on the Russian segments of the station [45.7]. The arm is 11.3 m long and has seven degrees of freedom. Its basic configuration and functionality are similar to SSRMS [45.8].

As a precursor demonstration of the ERA, the *German Aerospace Agency* (DLR) has developed a 0.5 m-long, two-degree-of-freedom manipulator arm with a dedicated test bench, called *robotic components verification on the ISS* (ROKVISS), see Fig. 45.5. ROKVISS was launched by an unmanned Russian Progress transport vehicle in 2004 and installed on the outer platform of the Russian segment of the station in early 2005 [45.9]. Although the number of joints is small, challenging experiments of telepresence have been conducted in which human operators on the ground operate the arm based on stereovision images and bilateral, high-fidelity force feedback using a force-reflecting joystick on the ground, and a joint torque control system on board. The secondary goal of the experiment was the space qualification of the joint drives, which are the key components of DLR's torque-controlled lightweight robots [45.10].

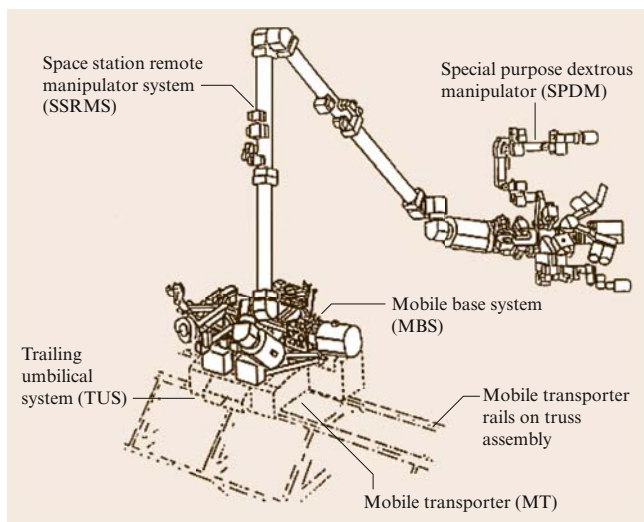


Fig. 45.4 Space station remote manipulator system (SSRMS) [45.4]

In Japan, the *Japanese experiment module remote manipulator system* (JEMRMS), shown in Fig. 45.6, has been developed by the *Japan space exploration agency* (JAXA) [45.11]. The arm will be attached to the Japanese module of the ISS. JEMRMS consists of two components: the main arm, a 9.9 m-long, six-degree-of-freedom arm and the small fine arm, a 1.9 m-long, six-degree-of-freedom arm. Unlike the SSRMS or the ERA, the main arm does not have self-relocation capability, but is fitted with a small fine arm, with which JEMRMS can form a serial 12-degree-of-freedom macro–micro manipulator system. After installation, the arm will be used to handle and relocate the components for the experiments and observations on the exposed facility [45.12, 13].

45.1.3 ROTEX

The *robot technology experiment* (ROTEX), developed by the German Aerospace Agency (DLR), is one of the important milestones of robotics technology in space [45.14]. A multisensory robotic arm was flown on the Space Shuttle COLUMBIA (STS-55) in 1993. Although the robot worked inside a work cell on the shuttle, several key technologies, such as a multisensory gripper, teleoperation from the ground and by the astronauts, shared autonomy, and time-delay compensation by the use of a predictive graphic display were successfully tested (Fig. 45.7).

45.1.4 ETS-VII

Engineering test satellite (ETS)-VII, shown in Fig. 45.8, was another milestone in the development of robotics technology in space, particularly in the area of satellite servicing. ETS-VII was an unmanned spacecraft developed and launched by the *National Space Development Agency of Japan* (NASDA, currently JAXA) in November 1997. A number of experiments were successfully conducted using a 2 m-long, six-degree-of-freedom manipulator arm mounted on its carrier (main) satellite.

The mission objective of ETS-VII was to test free-flying robotics technology and to demonstrate its utility in unmanned orbital operation and servicing tasks. The mission consisted of two subtasks: autonomous rendezvous/docking (RVD) and a number of robot experiments (RBT). The robot experiments included:

1. teleoperation from the ground with a large time delay
2. robotic servicing task demonstrations such as ORU exchange and deployment of a space structure

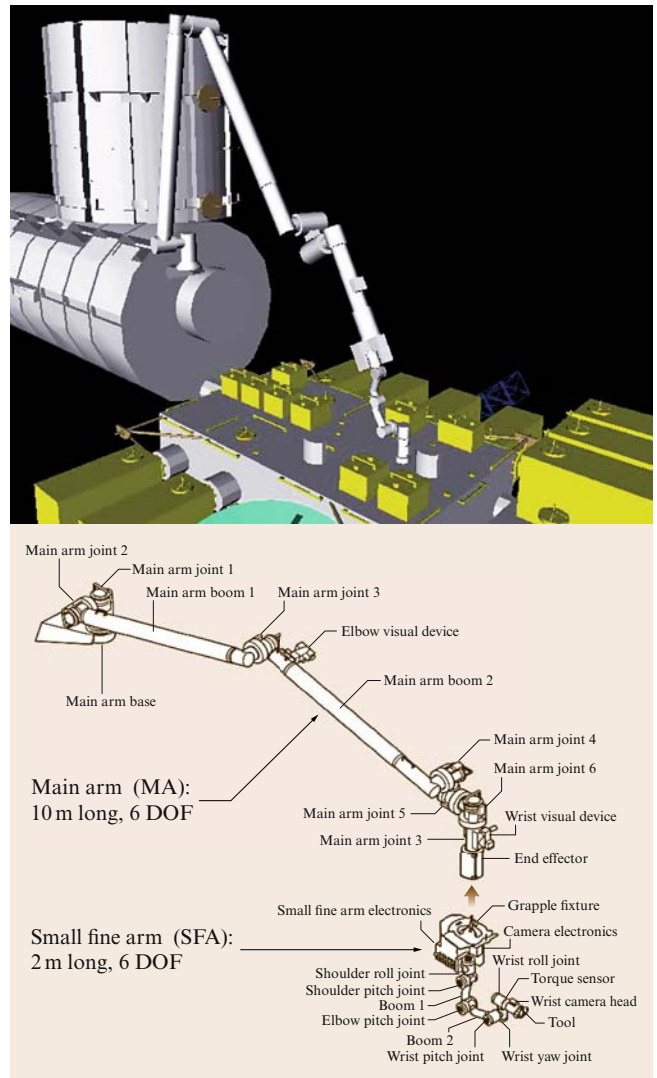


Fig. 45.6 Japan experiment module (JEM) on the ISS and the JEMRMS manipulator system

3. dynamically coordinated control between the manipulator reaction and the satellite attitude response
4. capture and berthing of a target satellite [45.15]

The communication time delay due to radio propagation (speed of light) is relatively small, for example, 0.25 s for a round trip to *geostationary Earth orbit* (GEO). However, to have a global coverage of communication in low-Earth-orbit operations, the signals are transmitted via multiple nodes including data relay satel-

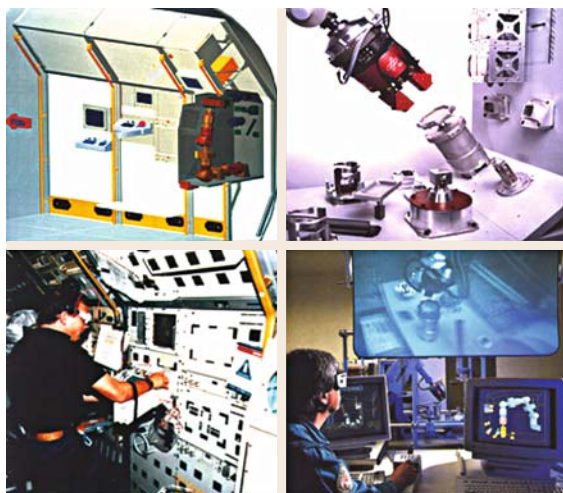


Fig. 45.7 ROTEX manipulator arm onboard the Spacelab D2 mission, the first remotely controlled space robot

lites located at GEO and ground stations. This makes the transmission distance longer, and even more additional delays are added at each node. As a result the cumulative delay becomes some seconds, actually 5–7 s in the case of the ETS-VII mission.

Opportunities for academic experiments were also opened to Japanese universities and European institutions (e.g., DLR and ESA) and important flight data were obtained that validate the concepts and theories for free-flying space robots [45.16, 17].

45.1.5 Ranger

Ranger is a teleoperated space robot being developed at the University of Maryland's Space Systems Lab-

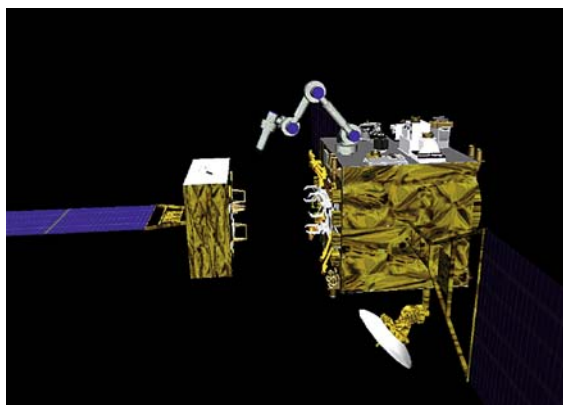


Fig. 45.8 Japanese engineering test satellite ETS-VII

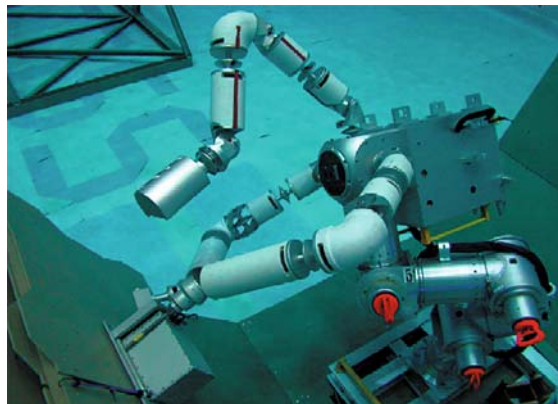


Fig. 45.9 Neutral buoyancy test of the Ranger telerobotic shuttle experiment

oratory [45.18]. Ranger consists of two seven-degree-of-freedom manipulators with interchangeable end-effectors to perform such tasks as changeout of *orbital replacement units (ORUs)* in orbit. Also discussed was the changeout of the *electronics controller unit (ECU)* of the Hubble space telescope, which previously required human EVA. A number of tests and demonstrations for servicing missions have been conducted at the University of Maryland neutral buoyancy facility (Fig. 45.9). Originally designed for a free-flying flight experiment, Ranger has been redesigned for a Space Shuttle experiment, but has not yet been manifested on a flight.

45.1.6 Orbital Express

The Orbital Express space operations architecture program is a DARPA program developed to validate the

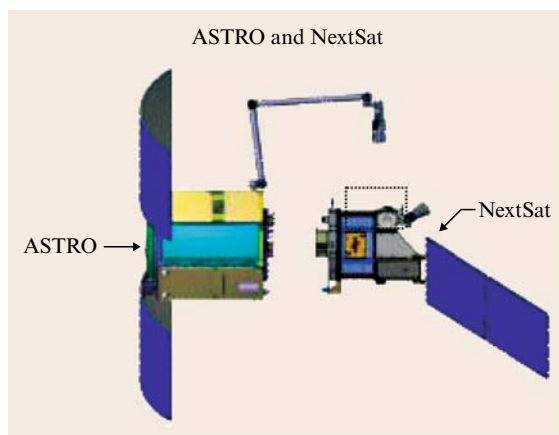


Fig. 45.10 Orbital Express flight mission configuration

technical feasibility of robotic on-orbit refueling and reconfiguration of satellites, as well as autonomous rendezvous, docking, and manipulator berthing [45.19]. The system consists of the *autonomous space transport robotic operations* (ASTRO) vehicle, developed by Boeing Integrated Defense Systems and a prototype modular next-generation serviceable satellite, NextSat, developed by Ball Aerospace. The ASTRO vehicle is equipped with a robotic arm to perform satellite capture and ORU exchange operations (Fig. 45.10).

After its launch in March 2007, various mission scenarios have been conducted. These scenarios include

1. visual inspection, fuel transfer, and ORU exchange on NextSat using ASTRO's manipulator arm when both spacecrafts are connected
2. separation of NextSat from ASTRO, orbital maneuvers by ASTRO and fly-around, rendezvous, and docking with NextSat
3. capture of NextSat using ASTRO's manipulator arm

These scenarios were successfully completed by July 2007, with ASTRO's onboard autonomy using onboard cameras and advanced video guidance system.

45.2 Historical Developments and Advances of Surface Robotic Systems

The research on surface exploration rovers began in the mid-1960s, with an initiative (that never flew) for an unmanned rover for the Surveyor lunar landers and a manned rover (Moon buggy) for the human landers in the United States. In the same period, research and development began for a teleoperated rover named Lunokhod in the Soviet Union. Both the Apollo manned rover and the Lunokhod unmanned rover were successfully demonstrated in the early 1970s on the Moon [45.20]. In the 1990s the exploration target had expanded to Mars and in 1997, the Mars Pathfinder mission successfully deployed a microrover named Sojourner that safely traversed the rocky field adjacent to the landing site by autonomously avoiding obstacles [45.21, 22]. Following on from this success, today autonomous robotic vehicles are considered indispensable technology for planetary exploration. The twin Mars exploration rovers, Spirit and Opportunity, were launched in 2003 and have had remarkable success in terms of remaining operational in the harsh environment of Mars for over four years. Each has traveled more than 5000 m and has made significant scientific discoveries using onboard instruments [45.23, 24].

45.2.1 Teleoperated Rovers

The first remotely operated robotic space surface vehicle was Lunokhod (Fig. 45.11) [45.20]. Lunokhod 1 landed on the Moon on 17 November 1970 as a payload on the lander Luna-17 and Lunokhod 2 landed on the Moon on 16 January 1973. Both were eight-wheeled skid-steered vehicles having a mass of about 840 kg, where almost all components were in a pressurized *bathtub* thermal enclosure with a lid that closed over the tub to allow it to survive the deep cold (≈ 100 K) of the long lunar

nights using only the heat emitted by small pellets of radioisotope. On the inside of the lid were solar arrays which recharged batteries during the day as required to maintain the operation of the vehicle. Lunokhod 1 operated for 322 Earth days, traversing over 10.5 km during that period and returned over 20 000 TV images, 200 high-resolution panoramas, and the results of more than



Fig. 45.11 Lunokhod

500 soil penetrometer tests and 25 soil analyses using its X-ray fluorescence spectrometer. Lunokhod 2 operated for about 4 months, having traversed more than 37 km, with the mission officially terminating on 4 June 1973. It has been reported that Lunokhod 2 was lost prematurely when it began sliding down a crater slope and hasty commands were sent in response which ultimately caused the end of the mission.

Each of the eight wheels on the Lunokhod vehicles were 0.51 m in diameter and 0.2 m wide, giving an effective ground pressure of less than 5 kPa based on an assumed sinkage of 3 cm. Each wheel had a brush-type direct-current (DC) motor, a planetary gear reduction, a brake and a disengagement mechanism allowing it to free-wheel in the event of some problem with the motor or gears. The mobility commands to the vehicle included two speeds forward or backward, braking, and turning to the right or the left either while moving or in place.

The vehicles had both gyroscope- and accelerometer-based tilt sensors which could automatically stop the vehicle in the event of excessive tilt of the chassis. Typical mobility commands specified a time duration over which the motors would run and then stop. Precision turning commands specified the angle through which the vehicle should turn. These commands were terminated when the specified turn angle had been reached according to the heading gyroscope. Odometry was determined by a ninth *small wheel* which was unpowered and lightly loaded and used only to determine over-the-ground distance. There was an onboard current-overload system and motor currents, pitch and roll measurements, and distance traversed and many component temperatures were telemetered to the ground operators.

The Lunokhod crew consisted of a driver, a navigator, a lead engineer, an operator for steering the *pencil-beam* communication antenna, and a crew commander. The driver viewed a monoscopic television image from the vehicle and gave the appropriate commands (*turn*, *proceed*, *stop* or *back up*) along with their associated parametric value in terms of duration or angle. The navigator viewed displays of telemetry from the vehicle's *course gyroscope*, *gyrovertical sensor*, and odometer and was responsible for calculating the trajectory of the vehicle and laying out the route to be followed. Thus the driver was responsible for vehicle stability about its center of mass and the navigator was responsible for the trajectory of that center of mass. The lead engineer (assisted by many specialists as required), was responsible for assessing the health of the onboard systems. The lead engineer provided both routine updates on energy supply, thermal conditions, etc. as well as possible

emergency alerts such as extreme motor currents or chassis tilt. The pencil-beam antenna operator oversaw the functioning of an independent ground-based closed-loop control system that servoed the antenna to always point at Earth, independent of the vehicle motion. The crew commander supervised the implementation and execution of the overall plan, gave any detailed commands for making actual contact with the surface (e.g., by the penetrometer) and also could override any command to the vehicle as he viewed the same information as the driver.

The entire driving system was tested extensively prior to the Lunokhod 1 mission at a *lunodrome* with simulated lunar terrain which proved to be more challenging than that actually encountered during the Lunokhod 1 mission. Despite this, the operators of Lunokhod 1 said they *encountered a dangerous situation* (unforeseen entrance into a crater, rolling onto a rock, etc.) slightly more often than once per kilometer. This was attributed to inadequate driving experience, the modest quality of the television images and the poor illumination conditions on the Moon. The driving direction was often selected primarily to give the best images; even so, the operators reported *fictional dangers* caused by varying illumination conditions. In the first three months (lunar days) of operation, the vehicle traversed 5224 m in 49 h of driving using 1695 driving commands, including about 500 turns. Sixteen signals were sent for protection against excessive tilt during that time; approximately 140 craters were traversed at maximum slope angles of 30°.

With the approximately 2.6 s speed-of-light delay, the operators stated that “control experience confirmed the desirability of movement in a starting–stopping regime with mandatory stopping each few meters.” The soil properties were found to “differ substantially even in terrain sectors not very distant from one another.” The soil penetrometer determined that the upper layer of regolith varied from a stiffest where the penetrometer required about 16 kg (Earth weight) of force to penetrate about 26 mm, to a weakest measurement where only 3 kg of Earth weight caused a penetration of about 39 mm. The cone penetrometer had a base diameter of 50 mm and a cone height of 44 mm. Thus the upper layer of regolith had a rate of increase of load-bearing strength ranging from about 400 kPa/m for the weakest soil to about 3 MPa/m for the stiffest soil. Crater walls and the immediate ejecta blanket around craters generally exhibited the weakest soil. Below 5–10 cm of penetration depth, the regolith generally became rapidly stiffer. The mean value of wheel slippage for the first three lunar days was about 10%. On horizontal terrain,

the slippage was 0–15%, depending on surface irregularities and ground inhomogeneity. On crater slopes the slip increased to 20–30%. The specific resistance of the Lunokhod wheels was generally in the range 0.05–0.25, while the specific free traction (the ratio of traction to weight) was in the range 0.2–0.41. The crater distribution in the area explored by Lunokhod 1 was found to be closely approximated by the formula $N(D) = AD^{-\delta}$, where $N(D)$ is the number of craters larger than diameter D meters per hectare of lunar surface, A is a scale factor found to be about 250 and δ is the distribution exponent, found to be about 1.4 [45.20].

45.2.2 Autonomous Rovers

In the mid-1960s, research began on a lunar rover at the [US Jet Propulsion Laboratory \(JPL\)](#) in Pasadena, California, when it was proposed to put a small rover on the Surveyor lunar landers. These landers were led by [JPL](#) (based on a system-level contract to Hughes) and were designed to land softly on the Moon to establish the safety of such a landing prior to the Apollo landers with humans aboard. At the time it was speculated (notably by T. Gold) that the Moon might be covered in a thick layer of soft dust that would *swallow* any lander. In 1963 [JPL](#) issued a contract to build a small rover concept prototype in support of the Surveyor program to the General Motors Defense Research Laboratories in Goleta, California. That GM facility had recently hired M.G. (Greg) Bekker, who was considered *the father of off-road locomotion*, having written several seminal textbooks on the subject and having introduced many of the key concepts relating soil properties to off-road vehicle performance that are still used today [45.25, 26] (Sect. 45.3.12).

Bekker and his team proposed an articulated six-wheeled vehicle based on a novel three-cab configuration with an axial spring-steel suspension. This vehicle exhibited remarkable mobility, being able to climb vertical steps up to three wheel radii high and crossing crevasses three wheel radii wide. Notable people working with Bekker were Farenc Pavlics, who went on to lead the development of the mobility system for the Apollo lunar rover (under contract from Boeing), and Fred Jindra, who developed the underlying equations describing the mobility of the six-wheeled articulated vehicle that were later used by Don Bickler in conceiving the *rocker bogie* chassis used on the Sojourner and the Mars exploration rovers. Bekker and his team proposed the six-wheeled articulated vehicle after experimenting with many types of vehicles, including multitracked ve-

hicles, screw-type vehicles (for fine-powdered terrain) and others. In scale-model testing the six-wheeled vehicle demonstrated superior performance over both soft and rocky terrain.

They built and delivered two vehicles that were about 2 m long with approximately 0.5 m wheel diameters. Those vehicles were used in testing throughout the 1960s and early 1970s to conduct simulated operations to determine how such vehicles could actually be used on the Moon. One key issue was that the speed-of-light round trip from the Moon (about 3 s) precluded direct *driving* of the vehicle. Perhaps most annoying was the fact that, during vehicle motion, the highly directional radio antenna used to communicate with Earth would lose its pointing and so communications would briefly be lost. This meant that operators driving the rover would be confronted with a series of still images, instead of a stream of moving images. It was quickly realized that much of an operator's *situation awareness* and depth perception needed to drive a vehicle with a monocular camera comes from motion. It was very difficult to drive from frozen monocular images. A crude form of stereo was incorporated where the camera mast was raised and lowered slightly and the operator could switch back and forth between the two views.

Following the successful landing of several of the Surveyor spacecraft and the discovery that all landing sites seemed to have relatively firm soil, it was concluded that the Surveyor lunar rover was not needed. As a result, the prototype was used for research into the early 1970s and subsequently restored for use again in research in the 1980s, becoming the first vehicle to be outfitted with *waypoint navigation* of the sort later used on the Sojourner and [MER](#) missions.

About the time that the stationary 1976 Viking landers were conceived and developed, [JPL](#) began the 1984 Mars Rover effort. (1984 was an energetically favorable launch opportunity from Earth to Mars and the next likely major mission opportunity after Viking.) Two test bed vehicles were developed, a *software* prototype and a *hardware* prototype. The software prototype had a *Stanford* arm, designed by Vic Scheinman (who went on to design the Unimation PUMA arm and many other famous early robotic devices). This was the only 1.5-scale Stanford arm ever built. Antal (Tony) *Beczcy* became well known in robotics for solving the kinematics of this arm, one of if not the first full kinematics ever done in robotics up to that time [45.27]. A stereo pan-tilt head was implemented, equipped with the first solid-state cameras to become available. A number of very important works were published in

the 1977 International Joint Conference on Artificial Intelligence [45.28]. The first *hand-eye locomotion* coordination was done with this vehicle, where a rock was designated in a stereo image and the vehicle maneuvered autonomously to a point where the arm could reach out and pick it up. One of the first demonstrations of *pin in hole* insertion and other *dexterous* manipulations were also done with this system in the 1970s.

The *hardware* prototype was built using elastic *loop wheels* made by *Lockheed* [45.29]. The vehicle was battery powered and controlled via a handheld remote-control (RC) unit of the type used by hobbyists.

In late 1982 the JPL had a contract with the US Army to study the use of robotic support vehicles. During this study, Brian Wilcox at JPL proposed a technique to reduce the need for a real-time video link or high-bandwidth communication channel between the vehicle and the operator. This technique (which became known as *computer-aided remote driving* or *CARD*) [45.30], re-

quired the transmission of a single stereo image from the vehicle to the operator, so the operator could designate waypoints in that image using a three-dimensional (3-D) cursor. By the use of a single stereo image instead of a continuous stream of monocular images, the amount of information that needed to be transmitted by the vehicle was reduced by orders of magnitude. JPL first demonstrated *CARD* on the resurrected *surveyor lunar rover vehicle* (SLRV, which had been painted baby-blue and so became known as the *Blue Rover*, see Fig. 45.12a), and later on a modified Humvee. During field tests in the Mojave desert Dn 1988, *CARD* was demonstrated on the Humvee with path designations of 100 m per stereo image and with time to designate each path of only a few seconds.

As the *CARD* work was ongoing, an internally funded effort at JPL demonstrated a concept called *semi-autonomous navigation* (SAN). This concept involved humans on Earth designating *global* paths using maps of the sort that could be developed from orbiter imagery and then having the vehicle autonomously refine and execute a *local* path that avoids hazards. The moderate success of that effort led to a NASA-funded effort, leading to the development of a new vehicle, called Robby (Fig. 45.12b). Robby was a larger vehicle that could support the onboard computing and power needed for untethered operation. (The SLRV had been tethered to a VAX 11/750 minicomputer over a 500 m tether during arroyo field testing of *CARD*.) For the first time (in 1990), an autonomous vehicle had made a traverse through an obstacle field that was faster than a rover could have done on Mars using human path designation done on Earth.

However, Robby had a severe *public relations* problem – it was perceived as too large. Of course none of the computers or power systems had been miniaturized or lightweighted – it was composed entirely of the lowest-cost components that could do the job. However, because it was the size of a large automobile, observers and NASA management got the impression that future rovers would be car-sized or even truck-sized vehicles. This was compounded by the *Mars rover sample return* (MRSR) study done by JPL in the late-1980s, which suggested a mass for the rover of 882 kg. An independent study of the MRSR study by Science Applications International, Inc. (SAIC) estimated the overall cost at \$13B. When word of this *outrageous* price tag filtered around NASA Headquarters and into the Congressional Staff, MRSR was summarily killed. Robby died along with it. At about the same time, NASA funded Carnegie Mellon University to develop *Ambler*

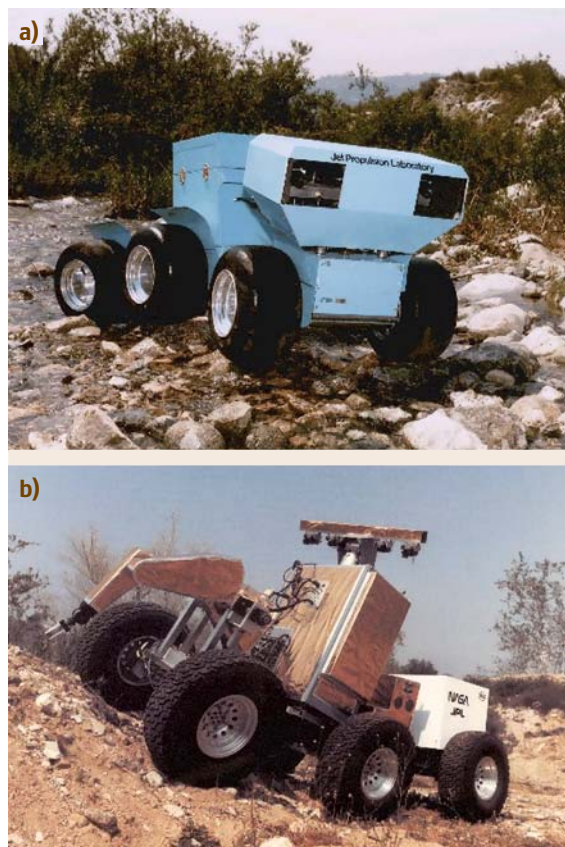


Fig. 45.12a,b Six-wheel articulated body rovers developed by JPL (a) SLRV and (b) Robby

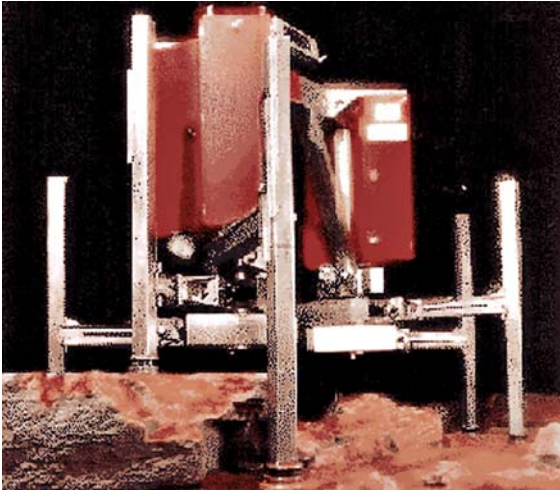


Fig. 45.13 Ambler

(Fig. 45.13), a large walking robot that was able to autonomously choose safe footfall locations, also as a test bed Mars Rover [45.31,32]. Ambler had a similar public-relations problem, being about the same mass as Robby, that the NASA management community was very skeptical that such large systems could affordably be flown to Mars. Both Robby and Ambler had all-onboard power and computing systems, which at that time were not sufficiently miniaturized to make autonomous rovers credible for actual flight missions. *Moore's law* was not only causing the computing technology to become miniaturized at a high rate, but also the energy required per computing instruction was dropping rapidly. This meant that early systems devoted most of their power to computing rather than to motive power. Later systems,

such as the Mars exploration rovers, have a more nearly equal balance between power for mobility and power for computation. Future systems will presumably devote the majority of their power to mobility as opposed to computation.

Soon thereafter, the *Mars environmental survey* (MESUR) mission set was proposed as a lower-cost alternative to a sample return mission. The MESUR Pathfinder mission was proposed as a first test of what was envisioned as a network of 16–20 surface stations to provide global coverage of Mars. A small rover was proposed to the Mars science working group [45.33,34]. A very short-term development effort culminated in a demonstration in July 1992 of a ≈ 4 kg rover that could move to directed points on the surface nearby a lander using stereo designation of waypoints in a 3-D display of frozen images taken from a lander mast camera pair (Fig. 45.14). This demonstration was sufficiently successful that a similar rover was manifested for the Mars Pathfinder mission. The Pathfinder rover (Fig. 45.15) was later named Sojourner, and became the first autonomous vehicle to traverse the surface of another planet, using a hazard detection and avoidance system to move safely between waypoints through a rock field [45.21, 22]. The hazard detection system avoided obstacles and was also used to position the vehicle accurately in front of rocks. Sojourner operated successfully for 83 Martian days (until the failure of the lander, which was acting as a communications relay between the rover and Earth). Sojourner examined approximately a dozen rock and soil samples with its alpha–proton–X-ray spectrometer, which gives the elemental composition of the rocks and soil. The success of Sojourner led directly to the decision to build the twin Mars exploration rovers



Fig. 45.14 Rocky 4



Fig. 45.15 The Pathfinder rover, Sojourner

launched in 2003. Both Sojourner and the MER rovers use waypoint designation in stereo images by the human operator together with autonomous hazard detection and avoidance to keep the rovers safe if they should wander off the designated path.

During the 1992–1993 summer season in Antarctica, the Dante I robot, built by Carnegie-Mellon University and funded by NASA, attempted to rappel into the caldera of the active volcano Mt. Erebus. Dante was a walking robot and was the first serious attempt to make a robot rappel down a grade that was too steep to traverse using purely frictional contact. Unfortunately, the extreme cold (even in the summer) compounded by human error caused a kink in the fiber-optic umbilical to snag going through an eyelet, breaking the high-bandwidth fiber communications on which the system depended. The fiber could not be repaired in the field and so the mission was aborted. Undaunted, in the summer of 1994, Dante II (Fig. 45.16) made a successful rappel into the caldera of Mt. Spurr in Alaska, exploring the active vents on the crater floor in a way that would be unsafe in the extreme if done by human explorers. The Dante robot series demonstrated that rappelling, especially when combined with legged locomotion, allows

robots to conduct exploration to extremely hazardous sites in ways that humans cannot.

In 1984 NASA started the Telerobotics Research program [45.35,36]. This program demonstrated various aspects of on-orbit assembly, maintenance, and servicing. Some highlights of this activity were the automated tracking and grapping of a free-spinning satellite (suspended with a counterweight and gimbal for realistic reactions under external forces), connection of a flight-like fluid coupler and many *busy box* functions such as door opening, threaded fastener mating and demating, use of power tools, dual-arm manipulation of a simulated hatch cover and flexible thermal blanket, etc. by various control approaches ranging from force-reflecting teleoperation to fully autonomous sequences. This activity ended in about 1990.

45.2.3 Research Systems

There have been many mobile robots built by government, university, and industrial groups whose objective was to develop new technologies for planetary surface exploration or to excite students or young engineers about the possibilities in that area. Carnegie Mellon University developed the Ambler, Dante, Nomad, Hyperion, Zoe, and Icebreaker robot series. The *Jet Propulsion Laboratory (JPL)*, Draper Labs, MIT, Sandia National Lab, and Martin-Marietta (later Lockheed-Martin) each built more than one planetary surface robot test bed. The Marsokhod chassis built by VNII Transmach of St. Petersburg, Russia was used by research groups there and also in Toulouse (LAAS and CNRS) [45.37, 38] as well as the NASA Ames Research Center and McDonnell Douglas Corporation (later part of the Boeing Company) in the US.

These research platforms have been used for two basic avenues of research. One is to perfect safe driving techniques on planetary surfaces, despite the speed-of-light latencies inherent in robotic exploration of the planets. This includes the waypoint navigation technology developed at JPL in the 1980s, where frozen stereo images are used to plan a possibly lengthy series of waypoints or activity sites and then executed with various sorts of reflexive hazard avoidance or safing techniques, such as used on the Sojourner rover on Mars in 1997. The other is to develop higher-level autonomy for improved science data return or mission robustness. Technologies in this latter category include mission planners that attempt to optimize routes and activity sequences based on time, limits to peak power, total energy, expected temperature, illumination angles, availability of



Fig. 45.16 Dante II at Mt. Spurr in Alaska

communications and others. Automated classification of possible science targets based on clustering of spectral data, figure-ground segmentation of rocks and other approaches have been attempted with some success. At the time of this writing some of these technologies have been uploaded to the twin Mars exploration rovers *Spirit* and *Opportunity* (Fig. 45.18) [45.23], including automated detection of temporary events of scientific interest such as dust-devils and clouds [45.39].

45.2.4 Sensing and Perception

In the 1980s, most planetary rover sensing research was based on laser ranging or stereo vision. Stereo vision was too computationally intensive for early low-power, radiation-hard processors, so the Sojourner Mars rover used a simple form of laser ranging to determine which areas were safe to traverse. Between the launch of Sojourner (1996) and the Mars exploration rovers (2003) sufficient progress had been made in radiation-hardened flight processors that stereo vision was used for hazard detection on Mars exploration rovers (*MER*) [45.40], mostly in experiments conducted with the Rocky-7 rover (Fig. 45.17). This allowed much larger numbers of range points to be incorporated into the hazard-detection algorithm (thousands of points, instead of the 20 discrete range points used by Sojourner). Perception of hazards on Sojourner was based on simple computations of average slope and roughness over the 4×5 array of range measurements, as well as the maximum height differences.

Each *MER* rover used a more sophisticated evaluation of the safety of the rovers along a large number of candidate arcs from its current location. Many other algorithms for the perception of terrain hazards have been used with reasonable success by various organizations. Today it is probably fair to say that the *unsolved problems* lie not in the area of geometric hazards (e.g., hazards that can be evaluated completely based on accurate knowledge of the shape of the terrain) but rather in the area of nongeometric hazards (e.g., hazards where uncertainties in the load-bearing or frictional properties of the terrain determine the safety of a proposed traverse). Accurate estimation of the load-bearing or friction properties of terrain by remote sensing is a very challenging task that will not be completely *solved* anytime soon, if ever.

45.2.5 Estimation

Most estimation for planetary surface exploration relates to the internal state of the robot or its position, pose, and



Fig. 45.17 Rocky 7

kinematic configuration with respect to the environment. Internal state sensors such as encoders on any active or passive articulations in the vehicle are used, along with a kinematic model and inertial sensors such as accelerometers and gyroscopes, to estimate the pose of the vehicle in inertial space. Perceptual algorithms such as surface reconstruction from clouds of range points as developed by stereo vision put terrain geometry estimates into this same representation. Heading in inertial space is generally the most difficult to estimate reliably, due to the lack of navigation aids such as the global positioning system or any easily measured heading reference such as a global magnetic field. Integration of rate-gyro data is used to maintain local attitude during motion while accu-



Fig. 45.18 The Mars exploration rovers, spirit and opportunity, with a manipulator arm in front

rate estimation of the rotation axis for Mars is possible by long integrations of three-axis rate-gyro data while the vehicle is stopped. Similar approaches are probably not feasible for the Moon, because of its slow rotation rate. Imaging of the solar disk or constellations of stars at precisely known times can be combined with stored models of the rotation of the planet to allow accurate estimation of the complete pose of the vehicle in inertial space. Kalman filtering or related techniques are generally employed to reduce the effects of measurement noise.

45.2.6 Manipulators for In Situ Science

The Mars exploration rovers were the first planetary exploration vehicles to have general-purpose manipulators. (Lunokhod had a single-purpose soil penetrometer and Sojourner had a single-degree-of-freedom device to place an alpha-proton-X-ray spectrometer in direct contact with the terrain.) The **MER** arms each have five degrees-of-freedom and a reach of over 1 m. Accurate gravity-sag models of the lightweight arm allow the precise position to be predicted in advance of any command to deploy an instrument and contact sensors allow the

arm to stop before any excessive forces build up in the relatively flexible arm. Future arms for planetary surface operations, especially any proposed assembly, maintenance or servicing tasks as part of the proposed lunar outpost, will require force sensing to protect the stronger but much more rigid arms from damage, as well as to allow controlled forces to be applied to workpieces. Of course there is a huge body of knowledge associated with industrial robot arms and undersea robotics (e.g., for the offshore oil industry), but such arms are generally very heavy, fast, and stiff compared with credible systems for planetary surface use. Delicate force control has rarely been applied to industrial settings. Space hardware is necessarily very lightweight and so both the arms and the workpieces will need to have well-resolved force sensing and control to prevent damage to one or both. Because of severe limits on both mass and power, space manipulation tends to be slow. Historically, this means the gear ratio between each motor and the corresponding output shaft is very large, making the use of motor current as an estimator for output torque very problematic. Other low-mass and robust means for accurate sensing of applied forces in the space environment are needed.

45.3 Mathematical Modeling

45.3.1 Space Robot as an Articulated-Body System

Broadly speaking, both on-orbit manipulators and surface mobile robots are considered to be common articulated body systems with a moving base. One point that clearly distinguishes them from other ground-based robots, such as industrial manipulators, is the existence of a moving base. The robotic systems discussed in this chapter consist of one or multiple articulated limbs mounted on a base body that has a dynamic coupling with these limbs. Typical styles of such moving base systems are categorized into the following groups [45.41].

Free-Floating Manipulator Systems

A space free-flyer that has one or more manipulator arms, as illustrated schematically in Fig. 45.19a, is a typical example of this group. When operating the manipulator arm(s), the position and orientation of the base spacecraft fluctuates due to the manipulator reaction. The kinetic momentum of the system is conserved if no external forces or moments are applied and the conservation law for this system governs the reaction

dynamics. Coordination or isolation between the base and manipulator dynamics is key to advanced motion control.

Macro-Micro Manipulator Systems

A robotic system that comprises a relatively small arm (micro arm) for fine manipulation mounted on a relatively large arm (macro arm) for coarse positioning, is called a macro-micro manipulator system. The **SSRMS** (Canadarm2) and the **SPDM** (Dextre) system, as well as the **JEMRMS** on the Japanese module of the **ISS**, are good examples. Here, the connecting interface at the end point of the macro arm or the root of the micro arm is modeled as the base body (Fig. 45.19b). A free-flying space robot may be treated in this group when its base body is actively controlled by actuators that produce external forces and moments, such as gas-jet thrusters. In this case, these actuators can be modeled as a virtual macro arm [45.42].

Flexible-Based Manipulator Systems

If the macro arm behaves as a passive flexible (elastic) structure in a macro-micro manipulator system, the

system is considered to be a flexible-based manipulator (Fig. 45.19c). Such a situation can be observed in the operation of the ISS, when the SSRMS is servo or brake locked after its coarse operation. Here, the issue is that the base body (the root of the micro arm or the end of the macro arm, according to the definition above) is subject to vibrations that will be excited by the reaction of the micro arm.

Mobile Robots with Articulated Limbs

Mobile robots for surface locomotion have the same structure in terms of the dynamics equation as the above groups. This group includes wheeled vehicles, walking (articulated limb) robots, and their hybrids. In a wheeled vehicle, suspension mechanisms, if any, are also modeled as articulated limb systems. The forces and moments yielded by contact with ground or planetary surface govern the motion of the system (Fig. 45.19d)

45.3.2 Equations for Free-Floating Manipulator Systems

Let us consider first a free-floating system with a single or multiple manipulator arm(s) mounted on a base spacecraft. The base body, termed link 0, is floating in inertial space without any external forces or moments. At the end point of the arm(s), external forces/moments may apply. For such a system, the equation of motion is expressed as follows

$$\begin{pmatrix} \mathbf{H}_b & \mathbf{H}_{bm} \\ \mathbf{H}_{bm}^\top & \mathbf{H}_m \end{pmatrix} \begin{pmatrix} \ddot{\mathbf{x}}_b \\ \ddot{\boldsymbol{\phi}} \end{pmatrix} + \begin{pmatrix} \mathbf{c}_b \\ \mathbf{c}_m \end{pmatrix} = \begin{pmatrix} \mathbf{0} \\ \boldsymbol{\tau} \end{pmatrix} + \begin{pmatrix} \mathbf{J}_b^\top \\ \mathbf{J}_m^\top \end{pmatrix} \mathbf{F}_h. \quad (45.1)$$

The kinematic relationship among \mathbf{x}_h , \mathbf{x}_b , and $\boldsymbol{\phi}$ is expressed using Jacobian matrices as

$$\dot{\mathbf{x}}_h = \mathbf{J}_m \dot{\boldsymbol{\phi}} + \mathbf{J}_b \dot{\mathbf{x}}_b, \quad (45.2)$$

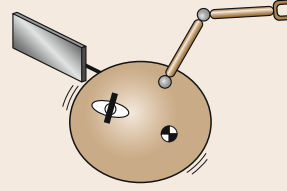
$$\ddot{\mathbf{x}}_h = \mathbf{J}_m \ddot{\boldsymbol{\phi}} + \dot{\mathbf{J}}_m \dot{\boldsymbol{\phi}} + \mathbf{J}_b \ddot{\mathbf{x}}_b + \dot{\mathbf{J}}_b \dot{\mathbf{x}}_b, \quad (45.3)$$

where the symbols are:

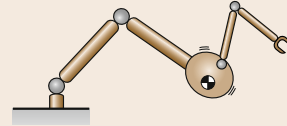
- $\mathbf{x}_b \in \mathbb{R}^6$: position/orientation of the base
- $\boldsymbol{\phi} \in \mathbb{R}^n$: joint angle of the arm
- $\mathbf{x}_h \in \mathbb{R}^{6k}$: position/orientation of the end point(s)
- $\boldsymbol{\tau} \in \mathbb{R}^n$: joint torque of the arm
- $\mathbf{F}_h \in \mathbb{R}^{6k}$: external forces/moments on the end point(s)
- n : number of total joints
- k : number of manipulator arms

and \mathbf{H}_b , \mathbf{H}_m , and \mathbf{H}_{bm} are inertia matrices for the base body, manipulator arm, and the coupling between

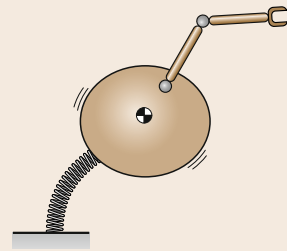
a) Free-floating manipulator system



b) Macro-micro manipulator system



c) Flexible structure based manipulator system



d) Surface locomotive robot system

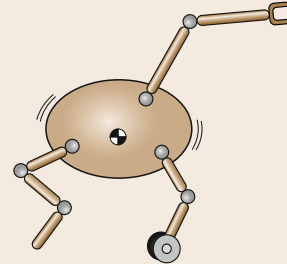


Fig. 45.19a–d Four basic types for moving base robots: (a) Free-floating manipulator system, (b) macro–micro manipulator system, (c) flexible-structure-based manipulator system, (d) surface locomotive robot system

the base and the arm, respectively, and \mathbf{c}_p and \mathbf{c}_q are nonlinear Coriolis and centrifugal forces, respectively.

For a free-floating manipulator in orbit, the gravity forces exerted on the system can be neglected and so the nonlinear term becomes $\mathbf{c}_b = \dot{\mathbf{H}}_b \dot{\mathbf{x}}_b + \dot{\mathbf{H}}_{bm} \dot{\boldsymbol{\phi}}$. Integrating the upper set of equation in (45.1) with respect to time, we obtain the total momentum of the system as

$$\mathcal{L} = \int \mathbf{J}_b^\top \mathbf{F}_h dt = \mathbf{H}_b \dot{\mathbf{x}}_b + \mathbf{H}_{bm} \dot{\boldsymbol{\phi}}. \quad (45.4)$$

For the case in which reaction wheels are mounted on the base body, they are included as additional manipulator arms.

45.3.3 Generalized Jacobian and Inertia Matrices

From (45.2) and (45.4), the coordinates of the manipulator base $\dot{\mathbf{x}}_b$, which are passive and unactuated coordinates, can be eliminated, as follows

$$\dot{\mathbf{x}}_h = \hat{\mathbf{J}}\dot{\boldsymbol{\phi}} + \dot{\mathbf{x}}_{h0}, \quad (45.5)$$

where

$$\hat{\mathbf{J}} = \mathbf{J}_m - \mathbf{J}_b \mathbf{H}_b^{-1} \mathbf{H}_{bm} \quad (45.6)$$

and

$$\dot{\mathbf{x}}_{h0} = \mathbf{J}_b \mathbf{H}_b^{-1} \mathcal{L}. \quad (45.7)$$

Since \mathbf{H}_b is the inertia tensor of a single rigid body (the manipulator base), it is always positive definite and so its inverse exists.

The matrix $\hat{\mathbf{J}}$ was first introduced in [45.43,44] and is referred to as the *generalized Jacobian matrix*. In its original definition, it was assumed that no external forces/moments acted on the system. If $\mathbf{F}_h = \mathbf{0}$, then the term $\dot{\mathbf{x}}_{h0}$ becomes constant and, in particular, if the system has zero initial momentum $\dot{\mathbf{x}}_{h0} = \mathbf{0}$, then (45.5) becomes simple. However, note that in the derivation of (45.6), zero or constant momentum is not a necessary condition.

Using this matrix, the manipulator hand can be operated under a resolved motion-rate control or resolved acceleration control in inertial space. Thanks to the generalized Jacobian, although the reactive base motion occurs during the operation, the hand is not disturbed by the reactive motion.

From the upper and lower sets of equations in (45.1), $\ddot{\mathbf{x}}_b$ can be eliminated to obtain the following expression

$$\hat{\mathbf{H}}\ddot{\boldsymbol{\phi}} + \hat{\mathbf{c}} = \boldsymbol{\tau} + \hat{\mathbf{J}}\mathbf{F}_h, \quad (45.8)$$

where

$$\hat{\mathbf{H}} = \mathbf{H}_m - \mathbf{H}_{bm}^T \mathbf{H}_b^{-1} \mathbf{H}_{bm}. \quad (45.9)$$

The matrix $\hat{\mathbf{H}}$ is known as the *generalized inertia matrix* for space manipulators [45.45]. This matrix represents the inertia property of the system in the joint space and can be mapped onto the Cartesian space using the generalized Jacobian matrix:

$$\hat{\mathbf{G}} = \hat{\mathbf{J}}\hat{\mathbf{H}}^{-1}\hat{\mathbf{J}}^T. \quad (45.10)$$

The matrix $\hat{\mathbf{G}}$ is referred to as the *inversed inertia tensor* for space manipulators and is useful for the discussion of impact dynamics when a space manipulator collides with or captures a floating target in orbit [45.46].

The *generalized jacobian matrix (GJM)* is a useful concept, with which the manipulator end point can perform positioning or trajectory tracking control by a simple control algorithm regardless of the attitude deviation during the operation.

A simplified laboratory demonstration was carried out using a two-dimensional free-floating test bed called *EFFORTS* [45.47]. To simulate the motion in a micro-gravity environment, a robot model was floated on a thin film of pressurized air on a horizontal plate, so that frictionless motion with momentum conservation was achieved.

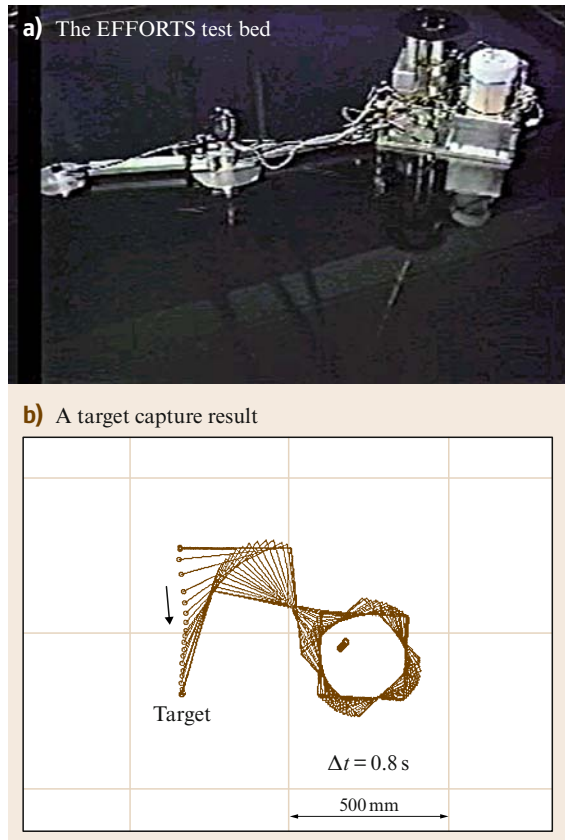


Fig. 45.20a,b Laboratory test bed for a free-floating space robot: (a) the EFFORTS test bed, (b) a target capture result

Figure 45.20 depicts the test bed and a typical experimental result. For Fig. 45.20b, the control command was given to the floating robot by

$$\dot{\phi} = \hat{J}^{-1} \dot{x}_d, \quad (45.11)$$

where \dot{x}_d is the desired velocity of the manipulator end point, the value of which was given and updated by online measurement of the end point position x_h and the target position x_t , as follows

$$\dot{x}_d = \frac{x_t - x_h}{\Delta t}, \quad (45.12)$$

where Δt is the time interval of the online control loop. The desired end point velocity was simply resolved into the joint velocity by (45.11).

The result clearly shows that the manipulator end point properly reached the target in an optimum manner, although the robot base rotated considerably due to the manipulator reaction. Note that, since the target was stationary in this example, the resulting motion trace was a straight line. However, thanks to the online control, the manipulator was also able to track and reach a moving target with the same control law.

The validity and effectiveness of the GJM-based manipulator control were also demonstrated in orbit by Japanese ETS-VII mission [45.16].

45.3.4 Linear and Angular Momenta

The integral of the upper set of equation in (45.1) gives a momentum equation, as shown in (45.4), which is composed of the linear and angular momenta. The linear part is expressed as

$$\tilde{H}_b v_b + \tilde{H}_{bm} \dot{\phi} = P, \quad (45.13)$$

where v_b is the linear velocity of the base, P is the initial linear momentum, and the inertia matrices with the over-cup are the corresponding components for the linear momentum [45.45]. When the linear momentum is further integrated, the result verifies the principle that the mass centroid of the entire system either remains stationary or translates with a constant velocity.

The angular momentum equation, however, does not have a second integral and therefore provides a first-order nonholonomic constraint [45.48]. The equation can be expressed as

$$\tilde{H}_b \omega_b + \tilde{H}_{bm} \dot{\phi} = L, \quad (45.14)$$

where ω_b is the angular velocity of the base, L is the initial angular momentum and the inertia matrices with the

over-tilde are the corresponding components for the angular momentum [45.45]. $\tilde{H}_{bm} \dot{\phi}$ represents the angular momentum generated by the manipulator motion.

Equation (45.14) can be solved for ω_b with zero initial angular momentum

$$\omega_b = -\tilde{H}_b^{-1} \tilde{H}_{bm} \dot{\phi}. \quad (45.15)$$

This expression describes the resulting disturbance motion of the base when there is joint motion $\dot{\phi}$ in the manipulator arm.

There are a number of points worth discussion when analyzing this equation. The magnitudes and directions of the maximum and minimum disturbances can be obtained from the singular value decomposition of the matrix $(-\tilde{H}_b^{-1} \tilde{H}_{bm})$ and displayed on the map. Such a map is called a *disturbance map* [45.49, 50]. Equation (45.15) is also used for the feedforward compensation in the coordinated manipulator–base control model [45.51, 52].

45.3.5 Virtual Manipulator

The concept of the *virtual manipulator (VM)* is an augmented kinematic representation that considers the base motion due to reaction forces or moments. The model is based on the fact that the mass centroid of the entire system does not move in the free-floating system without any external forces [45.53]. The mobility of the end point of the arm is decreased by the base motion. In the VM representation, such mobility degradation is expressed by virtually shrinking the length of the real arm according to the mass property. Note that the VM considers only conservation of linear momentum. If the differential expression of VM is obtained using a Jacobian matrix, the Jacobian is not a conventional kinematic Jacobian, but rather a version of the generalized Jacobian defined by the combination of the kinematic equation (45.2) and the linear momentum equation (45.13).

45.3.6 Dynamic Singularity

Dynamic singularities are singular configurations in which the manipulator end point loses mobility in some inertial direction [45.54]. Dynamic singularities are not found in Earth-based manipulators, but rather occur in free-floating space manipulator systems due to the coupling dynamics between the arm and the base. Dynamic singularities coincide with the singularities of the generalized Jacobian matrix determined by (45.6). The *singular value decomposition (SVD)*

of a manipulator Jacobian matrix provides *manipulability* analysis. Likewise, the SVD of the generalized Jacobian matrix yields the manipulability analysis of a free-floating space manipulator [45.55]. Figure 45.21 shows the comparison of the manipulability distribution between a two-degree-of-freedom (2-DOF) ground-based manipulator and a 2-DOF floating manipulator, from which the degradation of the manipulability is observed in the space arm due to the dynamic coupling.

45.3.7 Reaction Null Space (RNS)

From a practical point of view, any change in the base attitude is undesirable. As such, manipulator motion planning methods that minimize the base attitude disturbance have been investigated extensively. Analysis of the angular momentum equation reveals that the ultimate goal of achieving zero disturbance is possible.

The following is the angular momentum equation with zero initial angular momentum $\mathbf{L} = \mathbf{0}$ and the zero attitude disturbance $\omega_b = \mathbf{0}$ given in (45.14)

$$\tilde{\mathbf{H}}_{bm}\dot{\boldsymbol{\phi}} = \mathbf{0}. \quad (45.16)$$

This equation yields the following null-space solution

$$\dot{\boldsymbol{\phi}} = (\mathbf{E} - \tilde{\mathbf{H}}_{bm}^+ \tilde{\mathbf{H}}_{bm})\dot{\boldsymbol{\zeta}}, \quad (45.17)$$

where \mathbf{E} is an identity matrix. The joint motion given by this equation is guaranteed not to disturb the base attitude. Here, the vector $\dot{\boldsymbol{\zeta}} \in \mathbb{R}^n$ is arbitrary and the null space of the inertia matrix $\tilde{\mathbf{H}}_{bm} \in \mathbb{R}^{3 \times n}$ is called the *reaction null space (RNS)* [45.56].

The number of *degrees of freedom (DOF)* of $\dot{\boldsymbol{\zeta}}$ is $n - 3$. For example, if a manipulator arm mounted on

a free-floating space robot has six DOFs, i.e., $n = 6$, then three DOFs remain in the reaction null space. These DOFs can be specified by introducing additional motion criteria, such as end point positioning of the arm. Such manipulator operation that produces no reaction in the base is called *reactionless manipulation* [45.57].

The validity and effectiveness of the RNS-based reactionless manipulation were demonstrated in orbit by Japanese ETS-VII mission [45.16].

45.3.8 Equations for Flexible-Based Manipulator Systems

Next, let us consider a flexible-based manipulator system in which a single or multiple manipulator arm(s) are supported by a flexible-beam or a spring and damper (viscoelastic) system. For such a system, the equation of motion is obtained using the following variables

- $\mathbf{x}_b \in \mathbb{R}^6$: position/orientation of the base
- $\boldsymbol{\phi} \in \mathbb{R}^n$: joint angle of the arm
- $\mathbf{x}_h \in \mathbb{R}^{6k}$: position/orientation of the end point(s)
- $\mathbf{F}_b \in \mathbb{R}^6$: forces/moments to deflect the flexible base
- $\boldsymbol{\tau} \in \mathbb{R}^n$: joint torque of the arm
- $\mathbf{F}_h \in \mathbb{R}^{6k}$: external force/torque on the end point(s)

$$\begin{pmatrix} \mathbf{H}_b & \mathbf{H}_{bm} \\ \mathbf{H}_{bm}^\top & \mathbf{H}_m \end{pmatrix} \begin{pmatrix} \ddot{\mathbf{x}}_b \\ \ddot{\boldsymbol{\phi}} \end{pmatrix} + \begin{pmatrix} \mathbf{c}_b \\ \mathbf{c}_m \end{pmatrix} = \begin{pmatrix} \mathbf{F}_b \\ \boldsymbol{\tau} \end{pmatrix} + \begin{pmatrix} \mathbf{J}_b^\top \\ \mathbf{J}_m^\top \end{pmatrix} \mathbf{F}_h \quad (45.18)$$

$$\dot{\mathbf{x}}_h = \mathbf{J}_m \dot{\boldsymbol{\phi}} + \mathbf{J}_b \dot{\mathbf{x}}_b \quad (45.19)$$

$$\ddot{\mathbf{x}}_h = \mathbf{J}_m \ddot{\boldsymbol{\phi}} + \dot{\mathbf{J}}_m \dot{\boldsymbol{\phi}} + \mathbf{J}_b \ddot{\mathbf{x}}_b + \dot{\mathbf{J}}_b \dot{\mathbf{x}}_b. \quad (45.20)$$

Here, with the gravitational force \mathbf{g} in Cartesian space, the term \mathbf{c}_b is generally expressed as

$$\mathbf{c}_b = \mathbf{f}(\mathbf{x}_b, \boldsymbol{\phi}, \dot{\mathbf{x}}_b, \dot{\boldsymbol{\phi}}) + \mathbf{g}(\mathbf{x}_b, \boldsymbol{\phi}). \quad (45.21)$$

The difference from the equation of a free-floating manipulator system (45.1) is the existence of the base constraint force \mathbf{F}_b . Let \mathbf{D}_b and \mathbf{K}_b be the damping and spring factors, respectively, of the flexible base. The constraint forces and moments \mathbf{F}_b are then expressed as

$$\mathbf{F}_b = -\mathbf{D}_b \dot{\mathbf{x}}_b - \mathbf{K}_b \Delta \mathbf{x}_b, \quad (45.22)$$

where $\Delta \mathbf{x}_b$ denotes the elastic base displacement from its neutral position.

Since the base is constrained, the total momentum is not conserved and it might be meaningless to check the system momentum. However, it is important to consider the partial momentum \mathcal{L}_m for the part of the manipulator arm:

$$\mathcal{L}_m = \mathbf{H}_{bm} \dot{\boldsymbol{\phi}}, \quad (45.23)$$

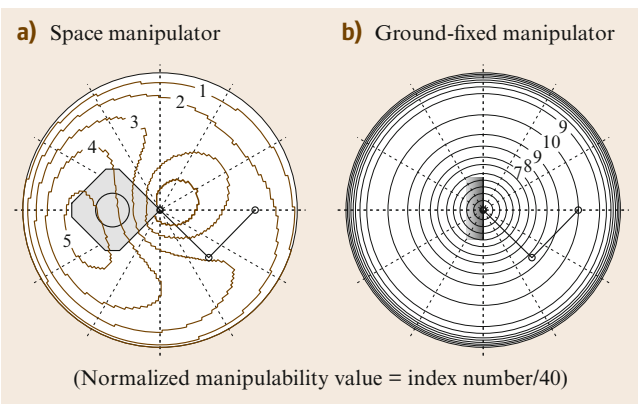


Fig. 45.21 Manipulability distribution in the work space

which is termed the *coupling momentum* [45.58]. Its time derivative describes the forces and moments \mathbf{F}_m , which are yielded by the dynamic reaction from the manipulator arm to the base

$$\mathbf{F}_m = \mathbf{H}_{bm}\ddot{\boldsymbol{\phi}} + \dot{\mathbf{H}}_{bm}\dot{\boldsymbol{\phi}}. \quad (45.24)$$

Using \mathbf{F}_b and \mathbf{F}_m , the upper set of equation in (45.18) is rearranged as

$$\mathbf{H}_b\ddot{\mathbf{x}}_b + \mathbf{D}_b\dot{\mathbf{x}}_b + \mathbf{K}_b\Delta\mathbf{x}_b = -\mathbf{g} - \mathbf{F}_m + \mathbf{J}_b^\top \mathbf{F}_h. \quad (45.25)$$

Equation (45.18) or (45.25), is a familiar expression for flexible-base manipulators [45.59, 60].

45.3.9 Advanced Control for Flexible Structure Based Manipulators

In this subsection, advanced control issues for a macro-micro space manipulator are discussed. The SSRMS attached to the SPDM (Fig. 45.4) and the JEMRMS (Fig. 45.6) are examples. Operation modes for this class of space manipulators include coarse motion by the macro (long-reach) component and fine manipulation by the micro component. In normal cases, these two control modes are executed exclusively. Namely, while one component is active the other component should be servo (or brake) locked. Thus, during the operation of the micro component, the macro component behaves just like a passive base.

Due to the flexible nature of the space long-reach arm, the macro part is subject to vibrations. These vibrations can be excited during coarse positioning and may remain for a long time after each operation. In fine manipulation, the macro arm behaves as a passive flexible structure, but then vibrations can be excited by reactions from the motion of the micro arm. These motions degrade the control accuracy and operational performance of the system. In practice, the booms are usually sufficiently stiff, but flexibility comes mainly from the low stiffness at the joints and gear trains. In addition, lightweight and microgravity characteristics make the structure sensitive to yield vibrations and the surrounding vacuum or the lack of air viscosity, provides a reduced damping effect to the structure.

Conventionally, the vibration issue has been managed by SRMS and SSRMS by the operational skill of well-trained astronauts and by limiting the maximum operational velocity according to the inertia of the handling object. However, if an advanced controller is introduced on the ISS, the training time for astronauts will be reduced and the operational speed can be increased.

Here, the following two subtasks are considered in dealing with this issue:

- suppression of the vibrations of the flexible base
- end point control in the presence of vibrations

To suppress the vibrations of the macro arm (flexible base), the coupled dynamics is effectively used. Such control is called *coupled vibration suppression control* [45.61]. The coupled dynamics is a solution space of the micro arm motion with maximum coupling with the vibration dynamics of the macro arm. Note that this solution space is perpendicular to the reaction null space introduced in Sect. 45.3.7. Since the spaces are orthogonal, the coupled vibration suppression control and reactionless manipulation can be superimposed without any mutual interference.

The motion command of the micro arm to suppress the vibrations is determined with a feedback of the linear and angular velocity of the end point of the macro arm $\dot{\mathbf{x}}_b$:

$$\ddot{\boldsymbol{\phi}} = \mathbf{H}_{bm}^+ \mathbf{H}_b \mathbf{G}_b \dot{\mathbf{x}}_b, \quad (45.26)$$

where $(\cdot)^+$ denotes the right pseudo-inverse and \mathbf{G}_b is a positive-definite gain matrix.

If written in the form of a joint torque input, the vibration control law is expressed as

$$\boldsymbol{\tau} = \mathbf{H}_m \mathbf{H}_{bm}^+ \mathbf{G}_b \dot{\mathbf{x}}_b. \quad (45.27)$$

In the presence of redundancy in the micro arm, (45.26) can be extended to control with a null-space component

$$\ddot{\boldsymbol{\phi}}_m = \mathbf{H}_{bm}^+ (\mathbf{H}_b \mathbf{G}_b \dot{\mathbf{x}}_b - \dot{\mathbf{H}}_{bm} \dot{\boldsymbol{\phi}}_m) + \mathbf{P}_{RNS} \boldsymbol{\zeta}, \quad (45.28)$$

where $\boldsymbol{\zeta}$ is an arbitrary n -DOF vector and $\mathbf{P}_{RNS} = (\mathbf{E} - \mathbf{H}_{bm}^+ \mathbf{H}_{bm})$ is a projector onto a null space of the coupling inertia matrix \mathbf{H}_{bm} . When the micro arm is operated using (45.28), the closed-loop system is expressed as

$$\mathbf{H}_b\ddot{\mathbf{x}}_b + \mathbf{H}_b \mathbf{G}_b \dot{\mathbf{x}}_b + \mathbf{K}_b \Delta\mathbf{x}_b = \mathbf{F}_b + \mathbf{J}_b^\top \mathbf{F}_h. \quad (45.29)$$

Equation (45.29) represents a second-order damped vibration system. With no force input, i. e., $\mathbf{F}_b = \mathbf{F}_h = 0$, the vibrations converge to zero with a proper choice of the gain matrix \mathbf{G}_b .

For the determination of the vector $\boldsymbol{\zeta}$, feedback control to reduce the positioning error of the micro arm end point is considered. The error vector is defined as

$$\tilde{\mathbf{x}}_h = \mathbf{x}_h^d - \mathbf{x}_h. \quad (45.30)$$

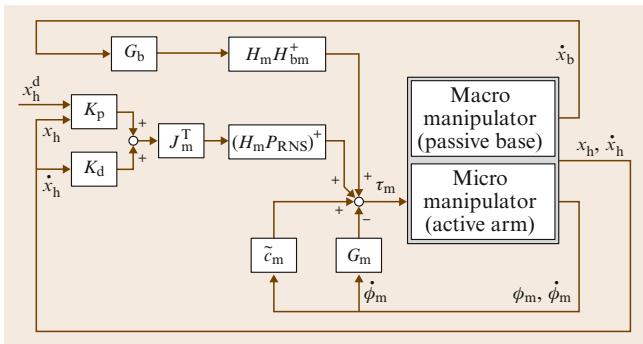


Fig. 45.22 Block diagram for simultaneous vibration suppression and manipulator end point control for a flexible-structure-mounted manipulator system

After some manipulation, the control law for the joint torque of the micro arm is obtained in the form [45.61, 62]

$$\tau = [(J_m^T)^+ H_m P_{RNS}]^+ (K_p \tilde{x}_h - K_d J_m \dot{\phi}) - G_m \dot{\phi}, \quad (45.31)$$

where K_p , K_d , and G_m are positive-definite gain matrices.

Figure 45.22 shows a block diagram for the control system described by Eqs. (45.27) and (45.31).

As a simplified demonstration, a planar system with a four-joint redundant manipulator arm atop a flexible beam is considered. Figure 45.23 shows the vibration amplitude of the flexible beam after an impulsive external force. The trace labeled 'w/o vs' depicts the vibrations of the beam without any manipulator control but with natural damping. The graph labeled 'with vs' depicts the case in which vibration suppression control given by (45.27) is applied, where the vibrations are damped quickly.

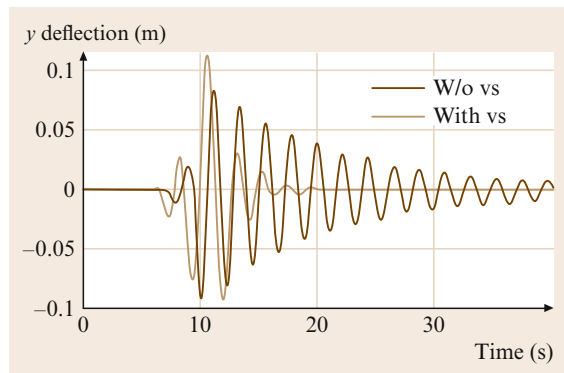


Fig. 45.23 Vibrations of the flexible base

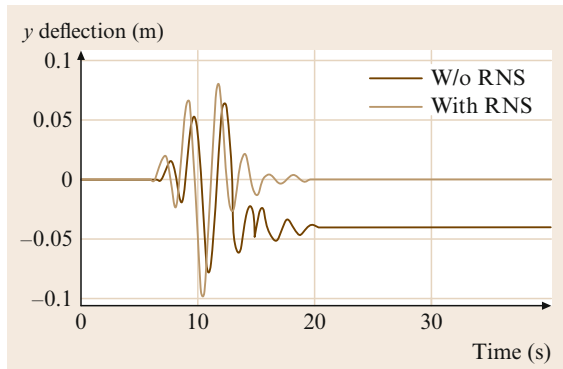


Fig. 45.24 Positioning error of the manipulator end tip

In addition, Fig. 45.24 shows the end point motion of the manipulator arm during the control. The graph labeled 'w/o RNS' is the case of using (45.27), where the base vibrations were successfully suppressed but the position of the manipulator end point was deflected by this suppression behavior. The graph labeled 'with RNS' depicts the case in which both vibration suppression control given by (45.27) and the end point control given by (45.31) are applied simultaneously. This last case shows that the vibrations were damped successfully and that the positioning error of the manipulator end point converged to zero. This is a result of the redundancy of the arm.

Here, note that the proposed control method requires precise information on dynamic characteristics, such as the inertia parameters of the arms and the handled payload, if any. To achieve more practical applications, the proposed method must be extended to schemes for parameter identification [45.63] and adaptive control [45.64], with which the convergence of the control is guaranteed even with imprecise a priori knowledge of the dynamic parameters [45.62].

45.3.10 Contact Dynamics and Impedance Control

The capture and retrieval operation of a floating and tumbling *target*, such as a malfunctioning satellite, by a manipulator arm mounted on a servicing robot (called a *chaser*) can be decomposed into the following three phases:

1. approach phase (before contact with the target)
2. contact/impact phase (at the moment of contact)
3. post-contact phase (after contact or grasping)

If the contact is impulsive, the first and the third phases are discontinued by the impulsive phenomena of the second phase. Understanding of this impulsive phenomena is indispensable when designing a comprehensive capture control scheme. In this subsection, the formulation of impact dynamics is first considered and impedance control (which is useful to minimize the impact forces and prolong the contact duration) is then discussed.

Let us consider a chain of rigid links composed of $n + 1$ bodies freely floating in inertial space. As discussed in Sect. 45.3.3, the equation of motion for this type of system becomes (45.8). Here, the impulsive contact force is assumed to yield at the manipulator end tip and is expressed as $\mathbf{F}_h = (\mathbf{f}_h^\top, \mathbf{n}_h^\top)^\top \in \mathbb{R}^6$. This impulsive force also yields a change in the system momenta $(\mathbf{P}_g^\top, \mathbf{L}_g^\top)^\top \in \mathbb{R}^6$, as expressed by

$$\begin{aligned} \begin{pmatrix} \dot{\mathbf{P}}_g \\ \dot{\mathbf{L}}_g \end{pmatrix} &= \begin{pmatrix} w\mathbf{E} & 0 \\ 0 & \mathbf{I}_g \end{pmatrix} \begin{pmatrix} \dot{\mathbf{v}}_g \\ \dot{\boldsymbol{\omega}}_g \end{pmatrix} + \begin{pmatrix} 0 \\ \boldsymbol{\omega}_g \times \mathbf{I}_g \boldsymbol{\omega}_g \end{pmatrix} \\ &= \begin{pmatrix} \mathbf{E} & 0 \\ \tilde{\mathbf{r}}_{gh} & \mathbf{E} \end{pmatrix} \begin{pmatrix} \mathbf{f}_h \\ \mathbf{n}_h \end{pmatrix}, \end{aligned} \quad (45.32)$$

where \mathbf{E} is a 3×3 identity matrix, w is a total mass, \mathbf{I} is an inertia matrix, and the symbols with the suffix ‘g’ indicate the corresponding values observed around the mass centroid of the $(n + 1)$ -link system.

In the above equations, (45.8) describes an internal joint motion (termed *local motion*) of the system, whereas (45.32) describes the overall motion (termed *global motion*) about the centroid of the system. As a result of force input \mathbf{F}_h , the floating chain induces both the local motion around its articulated joints and the global translation and rotation with respect to the centroid.

From (45.8) and (45.32), the acceleration of the manipulator end tip $\boldsymbol{\alpha}_h$ can be expressed in the inertial frame as

$$\boldsymbol{\alpha}_h = \mathbf{G}^* \mathbf{F}_h + \mathbf{d}^*, \quad (45.33)$$

where

$$\mathbf{G}^* = \hat{\mathbf{J}} \hat{\mathbf{H}}^{-1} \hat{\mathbf{J}}^\top + \mathbf{R}_h \mathbf{M}^{-1} \mathbf{R}_h^\top, \quad (45.34)$$

$$\mathbf{R}_h = \begin{pmatrix} \mathbf{E} & -\tilde{\mathbf{r}}_{gh} \\ 0 & \mathbf{E} \end{pmatrix}, \quad \mathbf{M} = \begin{pmatrix} w\mathbf{E} & 0 \\ 0 & \mathbf{I}_g \end{pmatrix}, \quad (45.35)$$

and \mathbf{d}^* is a velocity-dependent term.

Equations (45.33)–(45.35) are expressions for the motion of the hand (the point at which collision occurs) induced by the impact force \mathbf{F}_h , where the matrix \mathbf{G}^* , which is the augmented version of (45.10), represents the dynamic characteristics of this system.

Further augmentation for the inverted inertia matrix has been discussed for the case in which the contact duration is not considered to be infinitesimal [45.46].

Now let us assume the case in which two free-floating chains, A and B, with dynamic characteristics \mathbf{G}_A^* and \mathbf{G}_B^* collide with each other at their respective hands (end points) and an impact force \mathbf{F}_h is induced by this collision.

The equations of motion at the instance of collision are

$$\mathbf{G}_A^* \mathbf{F}_h = \begin{pmatrix} \dot{\mathbf{v}}_{hA} \\ \dot{\boldsymbol{\omega}}_{hA} \end{pmatrix} - \mathbf{d}_A^* \quad (45.36)$$

for chain A and

$$\mathbf{G}_B^* (-\mathbf{F}_h) = \begin{pmatrix} \dot{\mathbf{v}}_{hB} \\ \dot{\boldsymbol{\omega}}_{hB} \end{pmatrix} - \mathbf{d}_B^* \quad (45.37)$$

for chain B, where the subscripts A and B indicate the label of the chain.

Assuming that \mathbf{G}_A^* and \mathbf{G}_B^* remain constant during the infinitesimal contact duration and that the velocity-dependent terms \mathbf{d}_A^* and \mathbf{d}_B^* are small and negligible, integration of (45.36) and (45.37) yields

$$\mathbf{G}_A^* \int_t^{t+\delta t} \mathbf{F}_h dt = \begin{pmatrix} \mathbf{v}'_{hA} \\ \boldsymbol{\omega}'_{hA} \end{pmatrix} - \begin{pmatrix} \mathbf{v}_{hA} \\ \boldsymbol{\omega}_{hA} \end{pmatrix}, \quad (45.38)$$

$$\mathbf{G}_B^* \int_t^{t+\delta t} \mathbf{F}_h dt = \begin{pmatrix} \mathbf{v}_{hB} \\ \boldsymbol{\omega}_{hB} \end{pmatrix} - \begin{pmatrix} \mathbf{v}'_{hB} \\ \boldsymbol{\omega}'_{hB} \end{pmatrix}, \quad (45.39)$$

where $\{ \prime \}$ indicates the velocity after the collision. Integration of \mathbf{F}_h

$$\bar{\mathbf{F}}_h = \lim_{\delta t \rightarrow 0} \int_t^{t+\delta t} \mathbf{F}_h dt \quad (45.40)$$

represents the impulse (force-time product) acting on both chains. Providing that the total momenta of the two systems are strictly conserved before and after the collision, we obtain the following expression from (45.38) and (45.39).

$$\begin{aligned} (\mathbf{G}_A^* + \mathbf{G}_B^*) \bar{\mathbf{F}}_h &= \left[\begin{pmatrix} \mathbf{v}'_{hA} \\ \boldsymbol{\omega}'_{hA} \end{pmatrix} - \begin{pmatrix} \mathbf{v}'_{hB} \\ \boldsymbol{\omega}'_{hB} \end{pmatrix} \right] \\ &\quad + \left[\begin{pmatrix} \mathbf{v}_{hB} \\ \boldsymbol{\omega}_{hB} \end{pmatrix} - \begin{pmatrix} \mathbf{v}_{hA} \\ \boldsymbol{\omega}_{hA} \end{pmatrix} \right]. \end{aligned} \quad (45.41)$$

In general collision analysis, the coefficient of restitution (elasticity factor) associated with the relative

velocities before and after the collision is often employed [45.65]. If we accept this restitution coefficient for six-DOF linear and angular velocities, the relationship between relative velocities before and after contact becomes

$$\begin{pmatrix} v'_{hA} \\ \omega'_{hA} \end{pmatrix} - \begin{pmatrix} v'_{hB} \\ \omega'_{hB} \end{pmatrix} = \epsilon \left[\begin{pmatrix} v_{hB} \\ \omega_{hB} \end{pmatrix} - \begin{pmatrix} v_{hA} \\ \omega_{hA} \end{pmatrix} \right], \quad (45.42)$$

where

$$\epsilon \equiv \text{diag}(\epsilon_1, \dots, \epsilon_6) \quad 0 \leq \epsilon_i \leq 1 \quad (45.43)$$

is the restitution coefficient matrix.

Substituting (45.42) into (45.41), the impulse induced by this collision can be expressed only by the relative velocity of two points before the contact

$$\bar{F}_h = (E_6 + \epsilon) G_{\Sigma}^{*-1} v_{hAB}, \quad (45.44)$$

where

$$G_{\Sigma}^* = G_A^* + G_B^* \quad (45.45)$$

$$v_{hAB} = \begin{pmatrix} v_{hB} \\ \omega_{hB} \end{pmatrix} - \begin{pmatrix} v_{hA} \\ \omega_{hA} \end{pmatrix}. \quad (45.46)$$

Using the above notation, the magnitude of impulse is expressed as

$$\|\bar{F}_h\| = \sqrt{(E_6 + \epsilon)^T v_{hAB}^T G_{\Sigma}^{*-T} G_{\Sigma}^{*-1} v_{hAB} (E_6 + \epsilon)} \quad (45.47)$$

and the velocity after collision becomes

$$\begin{pmatrix} v'_{hA} \\ \omega'_{hA} \end{pmatrix} = (G_A^{*-1} + G_B^{*-1})^{-1} \left[(E_6 + \epsilon) G_B^{*-1} \begin{pmatrix} v_{hB} \\ \omega_{hB} \end{pmatrix} + (G_A^{*-1} - \epsilon G_B^{*-1}) \begin{pmatrix} v_{hA} \\ \omega_{hA} \end{pmatrix} \right], \quad (45.48)$$

where the suffixes A and B are interchangeable.

These expressions are considered to be an augmentation of the impact theory for a two-point-mass system into articulated body systems.

Impedance control is a concept by which to control the manipulator end tip so as to obtain the desired mechanical impedance characteristics. Such control is useful to alter the dynamic characteristics of the arm during the contact phase. In a special case, the desired impedance of the manipulator end tip (hand) may be tuned to achieve *impedance matching* with the colliding target object so that the hand can easily maintain stable contact with the target [45.66].

Let M_d , D_d , and K_d be matrices for the desired impedance properties of inertia, viscosity, and stiffness, respectively, measured at the manipulator end point. The equation of motion for the desired system is then expressed as

$$M_d \ddot{x}_h + D_d \dot{x}_h + K_d x_h = F_h. \quad (45.49)$$

From (45.8) and (45.49), the impedance control law for a free-floating manipulator system is obtained as follows [45.67]:

$$\tau_h = H^* \hat{J}^{-1} [M_d^{-1} (D_d \dot{x}_h + K_d x_h - F_h) - \dot{J} \dot{\phi} - \ddot{x}_{gh}] - \hat{J}^T F_h + c^*. \quad (45.50)$$

The usefulness of the impedance control in free-flying space robots has been discussed in [45.67–69].

45.3.11 Dynamics of Mobile Robots

The equation of motion for a mobile robot that has multiple articulated limbs, such as that shown in Fig. 45.25, is given by the following equation

$$\begin{pmatrix} H_b & H_{bm1} & \cdots & H_{bmk} \\ H_{bm1}^T & H_{m11} & \cdots & H_{m1k} \\ \vdots & \vdots & \ddots & \vdots \\ H_{bmk}^T & H_{m1k}^T & \cdots & H_{mkk} \end{pmatrix} \begin{pmatrix} \ddot{x}_b \\ \ddot{\phi}_1 \\ \vdots \\ \ddot{\phi}_k \end{pmatrix} + \begin{pmatrix} c_b \\ c_{m1} \\ \vdots \\ c_{mk} \end{pmatrix} = \begin{pmatrix} F_b \\ \tau_1 \\ \vdots \\ \tau_n \end{pmatrix} + \begin{pmatrix} J_b^T F_{ex} \\ J_{m1}^T F_{ex1} \\ \vdots \\ J_{mk}^T F_{exk} \end{pmatrix}, \quad (45.51)$$

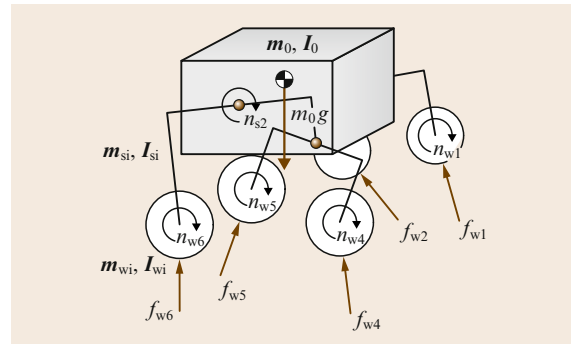


Fig. 45.25 Schematic model of a mobile robot

where the symbols have the following meanings

k :	number of limbs
$\mathbf{x}_b \in \mathbb{R}^6$:	position/orientation of the base
$\boldsymbol{\phi} = (\boldsymbol{\phi}_1^\top, \dots, \boldsymbol{\phi}_k^\top)^\top \in \mathbb{R}^n$:	articulated joint angles
$\mathbf{x}_{ex} = (\mathbf{x}_{ex1}^\top, \dots, \mathbf{x}_{exk}^\top)^\top \in \mathbb{R}^{6k}$:	position/orientation of the end points
$\mathbf{F}_b \in \mathbb{R}^6$:	forces/moments directly apply on the base
$\boldsymbol{\tau} = (\boldsymbol{\tau}_1^\top, \dots, \boldsymbol{\tau}_k^\top)^\top \in \mathbb{R}^n$:	joint articulated torque
$\mathbf{F}_{ex} = (\mathbf{F}_{ex1}^\top, \dots, \mathbf{F}_{exk}^\top)^\top \in \mathbb{R}^{6k}$:	external forces/moments on the end points

Note that for Fig. 45.25, $\mathbf{F}_{exi} = (\mathbf{f}_{wi}^\top, \mathbf{n}_{wi}^\top)^\top$.

Comparing the above equations with (45.1), no difference is observed in the mathematical structure. The gravity force on the vehicle main body and the configuration-dependent gravity terms of the articulated bodies are included in \mathbf{c}_b and \mathbf{c}_{mi} , respectively. In practice, however, one substantial difference is the existence of ground contact forces/moments at the end point of each limb. Unlike floating target capture discussed in Sect. 45.3.10, the contact is not considered impulsive, but instead continues for a nonnegligible period of time. In such cases, a well-accepted approach is to evaluate the contact forces/moments \mathbf{F}_{ex} explicitly, according to the virtual penetration of the end point into the collided object or the ground surface [45.65].

In cases in which each limb has a wheel on its end terminal, rather than the point penetration model, a wheel traction model shall be adopted to evaluate \mathbf{F}_{ex} . For planetary exploration missions, rovers (mobile robots) are expected to travel over natural rough terrain. A number of studies have examined the modeling of tire traction forces on loose soil, called *regolith* (where there is no organic component) [45.70–78].

In the following subsection, models for wheel traction mechanics are summarized.

45.3.12 Wheel Traction Mechanics

Terramechanics is the study of soil properties, specifically the interaction of wheeled, legged, or tracked vehicles and various surfaces. For the modeling of the wheel traction forces and the analysis of the vehicle mobility, textbooks written by *Bekker* [45.25, 26] and *Wong* [45.79] are good references. Although these books

were written in the 1960s and 1970s, basic formulae from these books are frequently cited by researchers even today [45.80]. In this subsection, the models for a rigid wheel on loose soil are summarized.

Slip Ratio and Slip Angle

Slips are generally observed when a rover travels on loose soil. In particular, slips in the lateral direction are observed during steering or slope-traversing maneuvers.

The slip in the longitudinal direction is measured by the slip ratio s , which is defined as a function of the longitudinal traveling velocity v_x of the wheel and the circumference velocity of the wheel $r\omega$ (r is the wheel radius and ω is the angular velocity of the wheel):

$$s = \begin{cases} (r\omega - v_x)/r\omega, & \text{if } |r\omega| > |v_x| : \text{driving}, \\ (r\omega - v_x)/v_x, & \text{if } |r\omega| < |v_x| : \text{braking}. \end{cases} \quad (45.52)$$

The slip ratio takes a value of from -1 to 1 .

On the other hand, the slip in the lateral direction is measured by the slip angle β , which is defined in terms of v_x and the lateral traveling velocity v_y as

$$\beta = \tan^{-1}(v_y/v_x). \quad (45.53)$$

Note that the above definitions, Eqs. (45.52) and (45.53), have traditionally been used in the vehicle community as standards. However, planetary rovers in a challenging terrain, such as Spirit and Opportunity on Mars, experienced the cases in which the rovers slip backward while attempting to drive up hill or travel faster than the wheel's circumference velocity in downhill driving. In these cases the slip ratio can exceed the range from -1 to 1 . Also while traversing side slopes, the case may arise in which $v_y > 0$ but v_x is nearly 0, making the definition (45.53) nearly singular. Therefore,

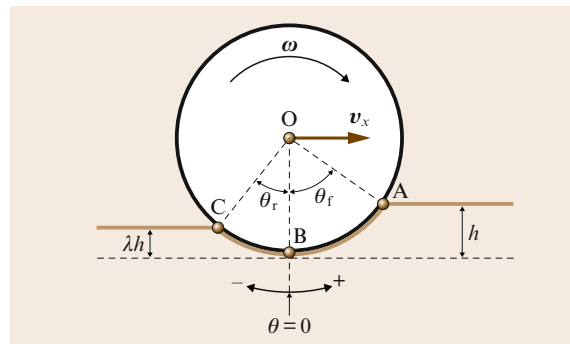


Fig. 45.26 Wheel contact angles

these definitions need to be further discussed for rovers in very loose terrain.

Wheel–Soil Contact Angle

Figure 45.26 depicts a schematic model of a rigid wheel contacting loose soil. In the figure, the angle from the surface normal to the point at which the wheel initially makes contact with the soil ($\angle AOB$) is defined as the entry angle. The angle from the surface normal to the point at which the wheel departs from the soil ($\angle BOC$ in Fig. 45.26) is the exit angle. The wheel contact region on loose soil is represented from the entry angle to the exit angle.

The entry angle θ_f is geometrically described in terms of wheel sinkage h as

$$\theta_f = \cos^{-1}(1 - h/r). \quad (45.54)$$

The exit angle θ_r is described using the wheel sinkage ratio λ , which denotes the ratio between the forward and rear sinkage of the wheel

$$\theta_r = \cos^{-1}(1 - \lambda h/r). \quad (45.55)$$

The value of λ depends on the soil characteristics, the wheel surface pattern and the slip ratio. It becomes

smaller than 1.0 when the soil compaction occurs, but can be greater than 1.0 when the soil is dug up by the wheel and transported to the rear region of the wheel.

Wheel Sinkage

The amount of wheel sinkage is constituted by static and dynamic components. The static sinkage depends on the vertical load on the wheel, while the dynamic sinkage is caused by the rotation of the wheel.

According to the equation formulated by Bekker [45.25], the static stress $p(h)$ generated under a flat plate, which has a sinkage h and a width b , is calculated as

$$p(h) = (k_c/b + k_\phi)h^n, \quad (45.56)$$

where k_c and k_ϕ are pressure-sinkage modules and n is the sinkage exponent. Applying (45.56) to the wheel, as shown in Fig. 45.27, the static sinkage is evaluated as follows.

First, the wheel sinkage $h(\theta)$ at an arbitrary wheel angle θ is geometrically given by

$$h(\theta) = r(\cos \theta - \cos \theta_s), \quad (45.57)$$

where θ_s is the static contact angle. Then, substituting (45.57) into (45.56) yields

$$p(\theta) = r^n(k_c/b + k_\phi)(\cos \theta - \cos \theta_s)^n. \quad (45.58)$$

The wheel eventually sinks into the soil until the stress from the soil balances the vertical load W on the wheel.

$$\begin{aligned} W &= \int_{-\theta_s}^{\theta_s} p(\theta) b r \cos \theta d\theta \\ &= r^{n+1} (k_c + k_\phi b) \int_{-\theta_s}^{\theta_s} (\cos \theta - \cos \theta_s)^n \cos \theta d\theta. \end{aligned} \quad (45.59)$$

Using this equation, the static contact angle θ_s is evaluated for the given W . In practice, (45.59) does not yield a closed-form solution for θ_s , although θ_s can be evaluated numerically.

Finally, the static sinkage h_s is obtained by substituting θ_s into the following equation

$$h_s = r(1 - \cos \theta_s). \quad (45.60)$$

However, as illustrated in Fig. 45.28, the dynamic sinkage becomes a complicated function depending on the slip ratio of the wheel, the wheel surface pattern, and the soil characteristics. Although it is difficult to obtain an analytical form for the dynamic sinkage, it is again

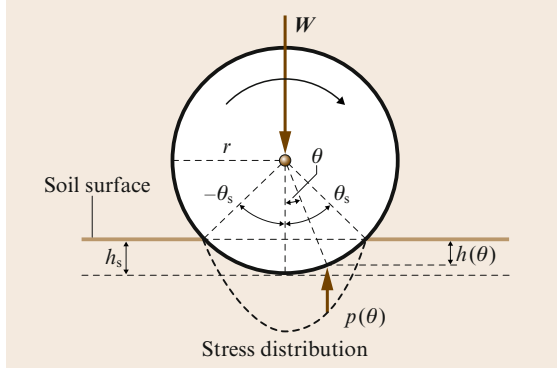


Fig. 45.27 Static sinkage

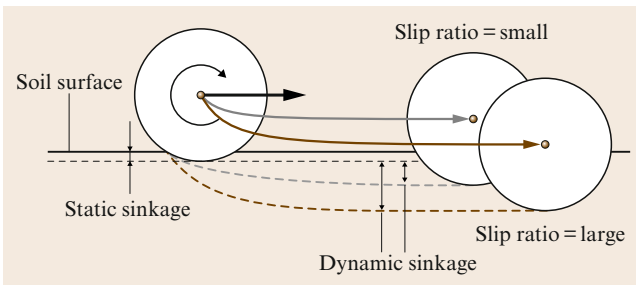


Fig. 45.28 Dynamic sinkage

possible to evaluate the dynamic sinkage numerically, using the condition $W = F_z$, where F_z is the normal force given by (45.71), which will be presented later herein. The force F_z increases with the wheel sinkage because the area of the contact patch increases accordingly.

Stress Distribution under the Wheel

Based on terramechanics models, the stress distribution under the rotating wheel can be modeled as shown in Fig. 45.29.

The normal stress $\sigma(\theta)$ is determined by the following equation [45.80, 81]:

$$\begin{aligned} \sigma(\theta) &= r^n \left(\frac{k_c}{b} + k_\phi \right) [\cos \theta - \cos \theta_f]^n \\ &\quad \text{for } \theta_m \leq \theta < \theta_f \\ \sigma(\theta) &= r^n \left(\frac{k_c}{b} + k_\phi \right) \left\{ \cos \left[\theta_f - \frac{\theta - \theta_r}{\theta_m - \theta_r} (\theta_f - \theta_m) \right] \right. \\ &\quad \left. - \cos \theta_f \right\}^n \quad \text{for } \theta_r < \theta \leq \theta_m \end{aligned} \quad (45.61)$$

Note that the above equations are based on Bekker's formula, as given in (45.56) and they become equivalent to the Wong–Reece model for normal stress [45.82] when $n = 1$. Note also that, by linearizing this distribution, Iagnemma et al. [45.70, 80] developed a Kalman-filter-based method to estimate the soil parameters.

The term θ_m is the specific wheel angle at which the normal stress is maximized

$$\theta_m = (a_0 + a_1 s) \theta_f, \quad (45.62)$$

where a_0 and a_1 are parameters that depend on the wheel–soil interaction. Their values are generally assumed to be $a_0 \approx 0.4$ and $0 \leq a_1 \leq 0.3$ [45.82].

The maximum terrain shear force is a function of the terrain cohesion c and internal friction angle ϕ and can be computed from Coulomb's equation

$$\tau_{\max}(\theta) = c + \sigma_{\max}(\theta) \tan \phi. \quad (45.63)$$

Based on the above equation, the shear stresses under the rotating wheel, $\tau_x(\theta)$ and $\tau_y(\theta)$, are written as [45.83]

$$\tau_x(\theta) = (c + \sigma(\theta) \tan \phi) (1 - e^{-j_x(\theta)/k_x}), \quad (45.64)$$

$$\tau_y(\theta) = (c + \sigma(\theta) \tan \phi) (1 - e^{-j_y(\theta)/k_y}), \quad (45.65)$$

where k_x and k_y are the shear deformation moduli in each direction. In addition, j_x and j_y , which are the

soil deformations in each direction, can be formulated as a function of the wheel angle θ with the slip ratio and the slip angle, respectively [45.73, 82]

$$j_x(\theta) = r[\theta_f - \theta - (1-s)(\sin \theta_f - \sin \theta)], \quad (45.66)$$

$$j_y(\theta) = r(1-s)(\theta_f - \theta) \tan \beta. \quad (45.67)$$

Drawbar Pull: F_x

Using the normal stress $\sigma(\theta)$ and the shear stress in the x direction $\tau_x(\theta)$, the drawbar pull F_x , which is the net traction force exerted from the soil to the wheel, is calculated as the integral from the entry angle θ_r to the exit angle θ_f [45.82]

$$F_x = rb \int_{\theta_r}^{\theta_f} \{ \tau_x(\theta) \cos \theta - \sigma(\theta) \sin \theta \} d\theta. \quad (45.68)$$

Side Force: F_y

The side force F_y appears in the lateral direction of the wheel when the vehicle makes steering maneuvers or traverses a side slope. The side force is decomposed into two components [45.63]

$$F_y = F_u + F_s,$$

where F_u is the force produced by the shear stress in the y direction $\tau_y(\theta)$ underneath the wheel and F_s is the reaction force generated by the bulldozing phenomenon on a side face of the wheel. The above equation can be

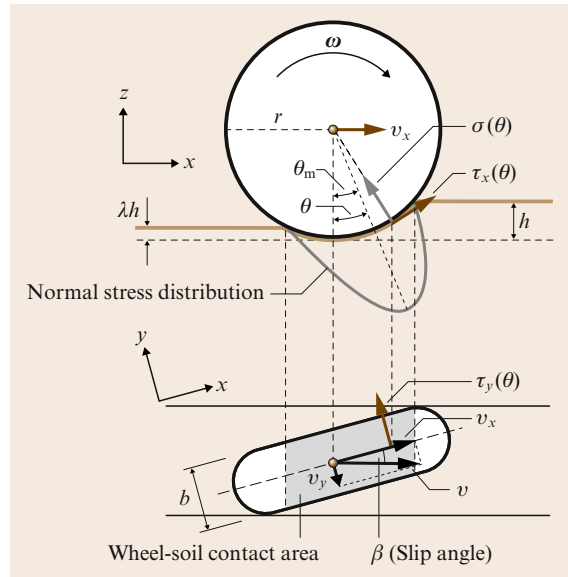


Fig. 45.29 Stress distribution model under a wheel

rewritten as

$$F_y = \int_{\theta_r}^{\theta_f} \underbrace{\{rb\tau_y(\theta)\}}_{F_u} + \underbrace{\{R_b[r - h(\theta)\cos\theta]\}}_{F_s} d\theta. \quad (45.69)$$

Here, *Hegedus's bulldozing resistance estimation* [45.84] is employed to evaluate the side face force F_s . As shown in Fig. 45.30, a bulldozing resistance R_b is generated on a unit width blade when the blade moves towards the soil. According to Hegedus's theory, the bulldozed area is defined by a destructive phase that is modeled by a planar surface. In the case of a horizontally placed wheel, the angle of approach α' should be zero. R_b can then be calculated as a function of wheel sinkage $h(\theta)$:

$$R_b(h) = D_1 \left[ch(\theta) + D_2 \frac{\rho_d h^2(\theta)}{2} \right], \quad (45.70)$$

where

$$D_1(X_c, \phi) = \cot X_c + \tan(X_c + \phi),$$

$$D_2(X_c, \phi) = \cot X_c + \cot^2 X_c / \cot \phi.$$

In the above equations, ρ_d denotes the soil density. Based on Bekker's theory [45.25], the destructive angle X_c can be approximated as

$$X_c = 45^\circ - \phi/2.$$

Normal Force: F_z

The normal force F_z is obtained in the same manner as for (45.68) [45.82]:

$$F_z = rb \int_{\theta_r}^{\theta_f} [\tau_x(\theta) \sin \theta + \sigma(\theta) \cos \theta] d\theta, \quad (45.71)$$

which should balance the normal load of the wheel in a static condition.

Motion dynamics simulation for a vehicle traveling over loose soil can be performed by substituting the forces F_x , F_y , and F_z obtained from the above equations into the equation of motion of (45.51).

A better understanding of the soil-wheel contact and traction mechanics is important in order to

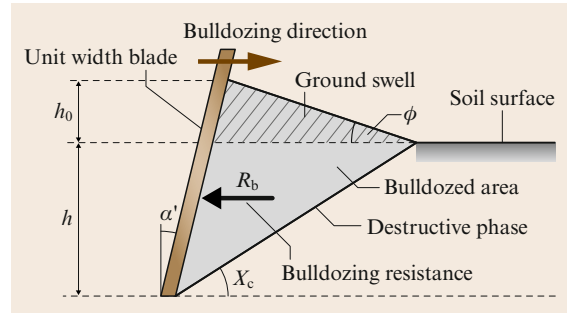


Fig. 45.30 Estimation model of the bulldozing resistance

improve the navigation and control behavior of exploration rovers, in terms of minimization of wheel slippage, for example. Reducing the wheel slippage will increase the power efficiency of surface locomotion, decrease the errors in path tracking maneuvers and decrease the risks of wheel spinning and sinking, which can cause immobilization of the vehicle.

One key to realizing such advanced control of slippage minimization is determining how to properly estimate the slip ratios and slip angles in real time using onboard sensors. The slip ratio is determined by the ratio between the wheel spinning velocity and the traveling velocity of the vehicle, but proper sensing of the velocity of the vehicle is usually difficult. One simple solution is to use a free wheel specialized for traveling velocity measurement. Another solution is to employ inertial sensors, which are however usually subject to noise and drift.

An alternative, but promising, possibility is visual odometry, which is based on optical flow or feature tracking in the sequence of optical images. Actually, this technique has been applied to the Mars exploration rovers, Spirit and Opportunity, in their long-range navigation, and there verified to be very useful. Particularly, the algorithm based on feature detection and tracking using a stereo pair of cameras provides reliable results with good accuracy for the estimation of driving distance as well as the wheel slippage [45.24].

45.4 Future Directions of Orbital and Surface Robotic Systems

45.4.1 Robotic Maintenance and Service Missions

Robotic maintenance and service missions for space infrastructure have been a long-term dream in the

space robotics community since their conceptual designs were first published in ARAMIS report in early 1980s (Fig. 45.1) [45.1].

ROTEX, ETS-VII, Ranger, and ASTRO, which were introduced in earlier sections, are technological devel-



Fig. 45.31 A conceptual drawing for robotic rescue of Hubble space telescope

opments toward this goal, but robotic maintenance and service missions have not become routinely operational yet. A good comparative study of orbital robotic missions is provided by [45.85]. The *Hubble space telescope* (HST) is a huge space telescope which has the capability to be serviced in orbit, but it has been visited by Space Shuttle and serviced (components exchanged and problems fixed) only by human EVA. After the COLUMBIA accident in 2003, NASA seriously considered the possibility of robotic maintenance of the HST, investigating available technologies and selecting a prime contractor of the mission development. Figure 45.31 depicts one possible configuration for the robotic rescue mission. Ultimately, it was decided to perform this last servicing mission with human astronauts. Maintenance of the HST involves tasks that are currently too complicated to be done by a robot, because the HST itself was designed for human-based maintenance and not specifically designed for robots.

Robonaut, which is described in the following subsection, is therefore considered as an interesting option for conducting practical maintenance and service missions due to its compatibility and similar level of dexterity as human astronauts.

45.4.2 Robonaut

Robonaut (Fig. 45.32a) is a humanoid robot designed by the Robot Systems Technology Branch at the NASA Johnson Space Center in a collaborative effort with DARPA. The Robonaut project seeks to develop and demonstrate a robotic system that can function as an EVA astronaut equivalent. Robonaut jumps generations ahead by eliminating the robotic scars (e.g., special

robotic grapples and targets), but it still keeps the human operator in the control loop through its telepresence control system. Robonaut is designed to be used for EVA tasks not specifically designed for robots [45.86].

A key challenge is to build machines that can help humans work and explore in space. Working side by side with humans or going where the risks are too great for people, machines like Robonaut will expand capabilities for construction and discovery. Over the past five decades, space flight hardware has been designed for human servicing. Space walks are planned for most of the assembly missions for the International Space Station and they are a key contingency for resolving on-orbit failures. To maintain compatibility with existing EVA tools and equipments, a humanoid shape and an assumed level of human performance (at least a human in a space suit) are required for this robotic surrogate.

The manipulator and dexterous hand have been developed with a substantial investment in mechatronics design. The arm structure has embedded avionics elements within each link, reducing cabling and noise interference. Robonaut has been designed based on a biologically inspired approach. For example, it uses a chordate neurological system in data management, bringing all feedback to a central nervous system, where even low-level servo control is performed. Such a biologically inspired approach is extended to left-right computational symmetry, sensor and power duality and kinematical redundancy, enabling learning and optimization in mechanical, and electrical and software forms.

Robonaut has a broad mix of sensors including thermal, position, tactile, force, and torque instrumentation, with over 150 sensors per arm. The control system for Robonaut includes an onboard, real-time central processing unit (CPU) with miniature data acquisition and power management. Off-board guidance is delivered with human supervision using a telepresence control station with human tracking.

One potential application of Robonaut is a regular monitoring and contingent maintenance work of human habitation modules of the space station. Fig. 45.32b, depicts such an application where Robonaut crawls on the surface of the station module by using hand rails which were originally designed for human EVA.

The application of Robonaut technology is not limited to orbital tasks. Figure 45.32c,d depicts conceptual designs at NASA and DLR, respectively, to combine the humanoid torso on a surface mobility system, which will be useful for robotic planetary explorations.

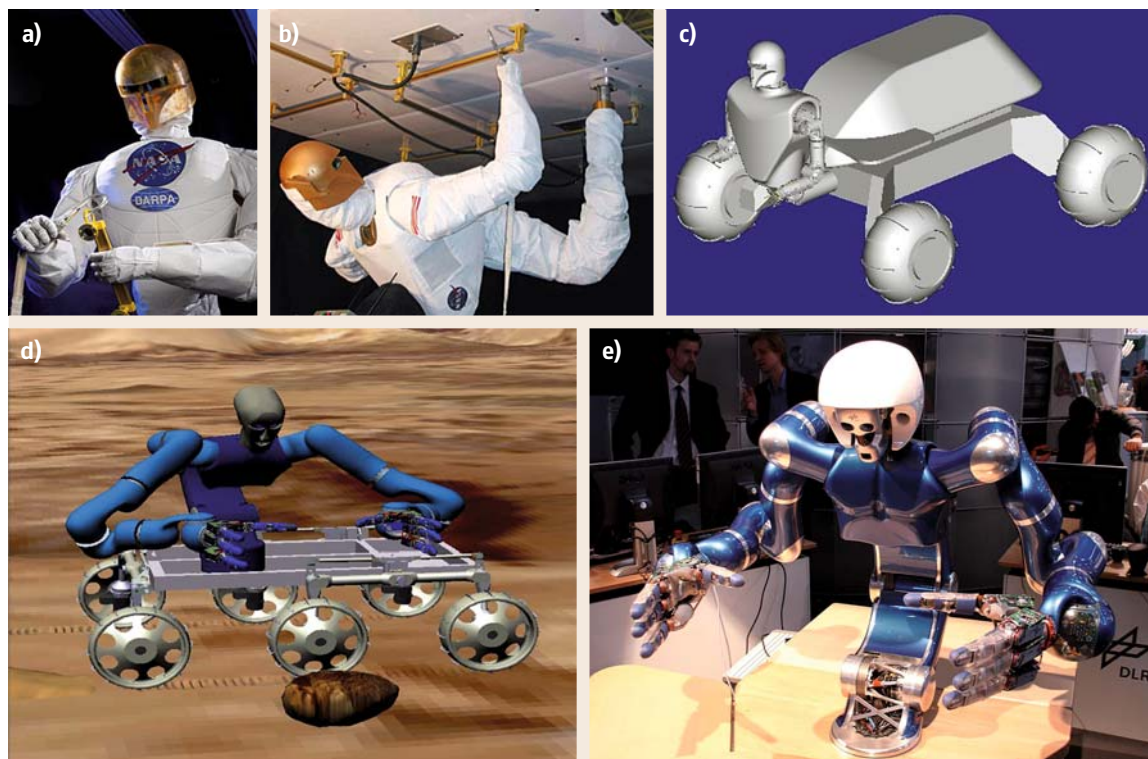


Fig. 45.32a–e Robonaut: (a,b) current model and future concepts by NASA (c), future concepts by DLR (d) which are based on the torso JUSTIN (e)

45.4.3 Aerial Platforms

There are three nonterrestrial planetary candidates for aerial robotic systems: Venus, Mars, and Titan (a moon of Saturn) [45.87, 88]. Venus has a very dense but hot atmosphere (460°C and 65 kg/m^3 at the surface) and so can easily float relatively heavy payloads. Mars has a very thin and cold atmosphere (somewhat variable but often -100°C and 0.02 kg/m^3). Titan has an atmosphere even colder than that of Mars ($\approx 100\text{ K}$) but about 50% denser than Earth's atmosphere. Thus very different vehicles have been envisioned for the three candidate mission targets. On Venus, buoyant devices are generally considered, especially those that can continuously or periodically rise high enough to reach moderate temperatures where conventional electronics can survive. One candidate is to use a phase-change fluid as part of the buoyant system, so that the fluid can condense in the cool upper atmosphere and be trapped in a pressure vessel, causing a loss of buoyancy and allowing the vehicle to descend, possibly all the way to the surface. After a brief stay and before the heat flux to the interior of

the device destroys all the sensitive equipment, a valve would be opened so that the phase-change fluid can evaporate, increasing the buoyancy and allowing the craft to ascend to the cool upper atmosphere. After a suitable period of heat rejection into this cool zone, the process can be repeated, perhaps indefinitely. The density of the Venus atmosphere is sufficiently high that powered dirigibles can be used, so that the buoyant vehicles can use propulsion and steering to reach particular locations in the atmosphere or on the surface [45.89].

In contrast, the Mars atmosphere is too thin for powered dirigibles to work (at least with the power-to-weight ratio of any current propulsion technology). Balloon aerobots could be deployed in the Mars atmosphere and could ascend and descend, but probably could not be steered precisely to specific locations, at least not by use of a propulsion system. Polar balloons could circumnavigate either pole many times or equatorial balloons could make one partial circuit around the planet, until they impact the *Tharsis Bulge*, a North-South string of high-altitude volcanoes that represents an essentially impenetrable barrier to any equatorial bal-

loon with a reasonable payload. Because of the problems with *lighter-than-air* vehicles in the thin Martian atmosphere, there has been considerable study of airplanes for use in exploring Mars. Aircraft can be designed to have reasonable lift-to-drag ratios in the Mars atmosphere, so that their performance is not too different from airplanes on Earth. Most often considered are gliders that deploy directly from an aeroshell that comes into the Mars atmosphere at hypersonic velocity and then proceed to glide hundreds or a thousand kilometers before impact. One common mission concept is to fly down the great Valles Marineris canyon, taking high-resolution imagery and spectrometry of the walls of that canyon. Powered aircraft have also been considered, including those that land and regenerate their propellant (e.g., using solar power and atmospheric CO₂) so as to be able to make multiple flights.

On Titan, like Venus, buoyant devices are generally considered most attractive (although helicopters have been proposed). Also like Venus, the atmosphere on Titan contains many obscuring particles and aerosols so that high-resolution imaging over a broad spectrum is only possible by getting close to the surface. This makes balloons or powered dirigibles very attractive. On Venus the extreme surface temperature makes it challenging to make a surface vehicle operate for an extended duration. On Titan, there is a significant risk that some sort of hydrocarbon *goo* exists on the surface that might foul any surface vehicle. Thus both Titan and Venus are considered especially attractive targets for the use of aerobots, especially in the form of powered dirigibles. Navigation of such aerobots would presumably be accomplished primarily by sensing the terrain and navigating relative to any landmarks that can be discerned. When these vehicles operate in the upper atmosphere, they can augment their position knowledge by means of sun or star tracking (as referenced to the local vertical). Deeper in the atmosphere, this may not be possible. One key issue is whether direct communications to Earth are envisioned or relay via satellite. If there is a satellite in orbit, it can provide considerable radio-navigation assistance and relatively frequent communications when the aerobot is on the side away from the Earth (both Venus and Titan spin very slowly). However, a satellite relay is expensive, so the least expensive options require that the dirigible have a large high-gain antenna (usually presumed to be inside the gas bag). Radio-based servo pointing at the Earth will provide precise navigation information (again along with precise measurements of local vertical). However, when the aerobot goes out of sight beyond the limb of the planet, it may spend days

or weeks out of communications with the Earth. This is probably the situation calling for the highest degree of autonomy of any that have been envisioned in robotic planetary exploration of the solar system.

45.4.4 Subsurface Platforms

Subsurface exploration of planetary bodies holds great promise: it is believed that a liquid-water aquifer may exist at significant depths on Mars, Europa, or Ganymede which probably represent the best possible locations within the solar system to look for extant (as opposed to extinct) extraterrestrial life. Also, in the lunar polar *dark craters* there is some evidence of the existence of water ice or other volatiles and there may exist a layered geologic record of impacts in the Earth–Moon system in these cold traps. Even access to a depth of a few meters holds the promise of reaching pristine scientific samples that have not been exposed to thermal cycling or ionizing radiation [45.90].

The prevailing wisdom has been that traditional sorts of drilling rigs are required to access these places, involving drill towers, multisegmented drill strings, large robotic systems to serve the function of a terrestrial drilling crew, and large power systems. Also, terrestrial drilling is usually done using large amounts of fluids (water, air or mud) to flush away cuttings and to cool and lubricate the cutter. The NASA Mars Technology Program has funded contractors that have demonstrated reaching 10 m of depth in a realistic setting with segmented drill strings without the use of fluids. While this is much less than needed to reach the putative liquid-water aquifers, it is much more than is reachable by previous techniques [45.91].

Other approaches have been proposed such as *moles* or *inchworms* that could be relatively self-contained and yet reach great depths without the mass and complexity of a large drill tower and segmented drill string. A key issue is that it appears that the needed energy cannot be stored onboard such self-contained drills, at least if it is stored as chemical energy. This is because drilling through terrain requires that some of the chemical bonds that hold the terrain together be broken and so if the energy of chemical bonds is used to provide that power, then a given volume of chemical energy storage can only advance some fixed ratio of its length into the terrain, where the ratio is determined by the efficiency in taking bond energies of one sort to break bonds of a different sort. Based on these considerations, it appears unlikely that a completely self-contained subsurface vehicle could advance more

than perhaps a hundred times its own length. Unless nuclear power sources are considered (and they have been), this requires some sort of tether to the surface to provide a nearly unlimited source of energy. Another problem for subsurface vehicles is that rock tends to expand when it is pulverized (in a process called *comminution*). Nonporous rock typically expands in volume by a few tens of percent when excavated, which means that fully self-contained subsurface vehicles have a severe *conservation of volume* problem. In principle the rock can be compressed back into its original volume, but this generally requires pressures much greater than the compressive strength of the original rock. The energy required to do this is much larger than the energy

required to excavate the rock in the first place and would become the dominant use of energy in an already energy-intensive effort.

As a result, it is generally assumed that any subsurface vehicle must keep some access tunnel open to the surface so that the excess volume of cuttings can be transported out. If this tunnel is available, then it seems that a means for getting power from the surface is also available, so that self-contained nuclear power is not needed. Subsurface vehicles with diameters as small as one or a few centimeters have been proposed that could potentially reach great depths within the mass and power constraints of feasible planetary robotic exploration missions.

45.5 Conclusions and Further Reading

Space robotics as a field is still in its infancy. The speed-of-light delays inherent to remote space operations makes the master–slave teleoperation approach that has been very useful in the undersea and nuclear industries problematic. Space robotics lacks the highly repetitive operations in a tightly structured environment that characterize industrial robotics. Hardware handled by space robots is very delicate and expensive. All three of these considerations have led to the fact that relatively few space robots have been flown, they have been very slow in operation, and only a small variety of tasks have been attempted. Nonetheless, the potential rewards of space robotics are great – exploring the solar system, creating vast space telescopes that may unlock the secrets of the universe, and enabling any viable space industries all seem to require major use of space robots. The scale of the solar system is not so great (a few

light-hours) that human intelligence cannot always supplement even the most remote space robot that becomes confused or stuck. Indeed, for the Moon (with only a few seconds of time delay) it seems that hazard avoidance and reliable closure of force–feedback loops is all that is required to make a highly useful robotic system. For Mars (with tens of minutes of time delay), along with hazard avoidance and force loop closure, it seems that robust anomaly detection (with modest reflexive *safing* procedures) and perhaps scientific-novelty detection are probably all that is needed. High levels of autonomy are enhancing but not enabling for work in the inner solar system and become more and more desirable for robots that are sent farther into the outer solar system.

For further reading, the following materials are suggested [45.92–97].

References

- 45.1 D. L. Akin, M. L. Minsky, E. D. Thiel, C. R. Curtzman: Space applications of automation, robotics and machine intelligence systems (ARAMIS) phase II, NASA-CR-3734-3736 (1983)
- 45.2 C.G. Wagner-Bartak, J.A. Middleton, J.A. Hunter: Shuttle remote manipulator system hardware test facility, 11th Space Simulation Conf. (1980) pp. 79–94, NASA CP-2150
- 45.3 S. Greaves, K. Boyle, N. Doshewnek: Orbiter boom sensor system and shuttle return to flight: operations analyses, AIAA Guidance Navigation Contr. Conf. Exhibit (San Francisco 2005) p. 5986
- 45.4 C. Crane, J. Duffy, T. Carnahan: A kinematic analysis of the space station remote manipulator system (SSRMS), J. Robot. Syst. **8**, 637–658 (1991)
- 45.5 M.F. Stieber, C.P. Trudel, D.G. Hunter: Robotic systems for the international space station, Proc. 1997 IEEE Int. Conf. Robot. Autom. (1997) pp. 3068–3073
- 45.6 D. Bassett, A. Abramovici: Special purpose dexterous manipulator (SPDM) requirements verification, Proc. 5th Int. Symp. Artif. Intell. Robot. Autom. Space (1999) pp. 43–48, ESA SP-440
- 45.7 R. Boumans, C. Heemskerk: The european robotic arm for the international space station, Robot. Auton. Syst. **23**(1), 17–27 (1998)

- 45.8 P. Laryssa, E. Lindsay, O. Layi, O. Marius, K. Nara, L. Aris, T. Ed: International space station robotics: a comparative study of ERA, JEMRMS and MSS, Proc. 7th ESA Workshop Adv. Space Technol. Robot. Autom. ASTRA (ESTEC, Noordwijk 2002)
- 45.9 C. Preusche, D. Reintsema, K. Landzettel, G. Hirzinger: Robotics component verification on iss rokviss – preliminary results for telepresence, Proc. IEEE/RSJ Int. Conf. Intell. Robot. Syst. (Beijing 2006) pp. 4595–4601
- 45.10 K. Landzettel, A. Albu-Schaffer, C. Preusche, D. Reintsema, B. Rebele: G. Hirzinger: Robotic on-orbit servicing – dlr's experience and perspective, Proc. of IEEE/RSJ Int. Conf. Intell. Robot. Syst. (Beijing 2006) pp. 4587–4594
- 45.11 T. Matsueda, K. Kuraoka, K. Goma, T. Sumi, R. Okamura: JEMRMS system design and development status, Proc. IEEE National Telesyst. Conf. (1991) pp. 391–395
- 45.12 S. Doi, Y. Wakabayashi, T. Matsuda, N. Satoh: JEM remote manipulator system, J. Aeronaut. Space Sci. Japan **50**(576), 7–14 (2002)
- 45.13 H. Morimoto, N. Satoh, Y. Wakabayashi, M. Hayashi, Y. Aiko: Performance of Japanese robotic arms of the international space station, 15th IFAC World Congress (2002)
- 45.14 G. Hirzinger, B. Brunner, J. Dietrich, J. Heindl: Sensor-based space robotics–ROTEX and its telerobotic features, IEEE Trans. Robot. Autom. **9**(5), 649–663 (1993)
- 45.15 M. Oda et al.: ETS–VII, space robot in-orbit experiment satellite, Proc. 1996 IEEE Int. Conf. Robot. Autom. (1996) pp. 739–744
- 45.16 K. Yoshida: Engineering test satellite vii flight experiments for space robot dynamics and control: theories on laboratory test beds ten years ago, now in orbit, Int. J. Robot. Res. **22**(5), 321–335 (2003)
- 45.17 K. Landzettel, B. Brunner, G. Hirzinger, R. Lampariello, G. Schreiber, B.–M. Steinmetz: A unified ground control and programming methodology for space robotics applications – demonstrations on ETS–VII, Proc. Int. Symp. Robot. (Montreal 2000) pp. 422–427
- 45.18 J.C. Parrish, D.L. Akin, G.G. Gefke: The ranger telerobotic shuttle experiment: implications for operational EVA/robotic cooperation, Proc. SAE Int. Conf. Environmental Syst. (Toulouse 2000)
- 45.19 J. Shoemaker, M. Wright: Orbital express space operations architecture program. Space systems technology and operations, Proc. SPIE, Vol. 5088, ed. by P. Tchoryk Jr., J. Shoemaker, (2003) pp. 1–9
- 45.20 A.P. Vinogradov: *Lunokhod 1 Mobile Lunar Laboratory* (JPRS, Moscow 1971), JPRS identification number 54525
- 45.21 A. Mishkin: *Sojourner: An Insider's View of the Mars Pathfinder Mission* (Berkley Books, New York 2004)
- 45.22 B. Wilcox, T. Nguyen: Sojourner on mars and lessons learned for future planetary rovers, 28th Int. Conf. Env. Syst. (Danvers 1998)
- 45.23 M. Maimone, A. Johnson, Y. Cheng, R. Willson, L. Matthies: Autonomous navigation results from the Mars exploration rover (MER) mission, Proc. 9th Int. Symp. Experimental Robot. (ISER) (Singapore 2004)
- 45.24 M. Maimone, Y. Cheng, L. Matthies: Two years of visual odometry on the Mars exploration rovers, J. Field Robot. **24**(3), 169–186 (2007)
- 45.25 M.G. Bekker: *Off-The-Road Locomotion* (Univ. Michigan Press, East Lausing 1960)
- 45.26 M.G. Bekker: *Introduction to Terrain-Vehicle Systems* (Univ Michigan Press, East Lausing 1960)
- 45.27 R.A. Lewis, A.K. Bejczy: Planning considerations for a roving robot with arm, IJCAI (1973) pp. 308–316
- 45.28 A. Thompson: The navigation system of the JPL robot, IJCAI (1977) pp. 749–757
- 45.29 E. J. M. West, W. Trautwein: Operational Loopwheel Suspension Systems for Mars Rover Demonstration Model Loopwheel failure report. Document LMSC-HREC TR D568859, (Huntsville Research & Engineering Center, Huntsville 1979) Available at http://ntrs.nasa.gov/archive/nasa/casi.ntrs.nasa.gov/19790011992_1979011992.pdf
- 45.30 Y. Yakimovsky, R.T. Cunningham: A system for extracting three-dimensional measurements from a stereo pair of TV cameras, Comp. Graph. Image Proc. **7**, 195–210 (1978)
- 45.31 E. Krotkov, J. Bares, T. Kanade, T. Mitchell, R. Simmons, W. Whittaker: Ambler: a six-legged planetary rover, 5th Int. Conf. Adv. Robot. 1991 Robots Unstructured Env., Vol. 1 (1991) pp. 717–722
- 45.32 J. Bares, W. Whittaker: Walking robot with a circulating gait, Proc. IEEE/RSJ Int. Conf. Intell. Robot. Syst. Towards New Frontier Appl. (IROS '90), Vol. 2 (1990) pp. 809–816
- 45.33 B. Wilcox, D. Gennery: A Mars rover for the 1990s, J. Br. Interplanet. Soc. **40**, 484–488 (1987)
- 45.34 B. Wilcox, L. Matthies, D. Gennery: Robotic vehicles for planetary exploration, Proc. Int. Conf. Robot. Autom. (Nice 1992)
- 45.35 D. Gennery, T. Litwin, B. Wilcox, B. Bon: Sensing and perception research for space telerobotics at JPL, IEEE Int. Conf. Robot. Autom. (Raleigh 1987) pp. 311–317
- 45.36 J. Balaram, S. Hayati: A supervisory telerobotics testbed for unstructured environments, J. Robot. Syst. **9**(2), 261–280 (1992)
- 45.37 G. Giral, L. Boissier: The French planetary rover VAP: concept and current developments, IEEE Int. Conf. Intell. Robot. Syst. (IROS'92) (Raleigh 1992) pp. 1391–1398, LAAS Report No. 92227
- 45.38 R. Chatila, S. Lacroiz, G. Giral: A case study in machine intelligence: adaptive autonomous space rovers, Int. Conf. Field Service Robot. (FSR'97) (Cannberra 1997) pp. 101–108, LAAS Report No. 97463

- 45.39 A. Castano, A. Fukunaga, J. Biesiadecki, L. Neakrase, P. Whelley, R. Greeley, M. Lemmon, R. Castano, S. Chien: Autonomous detection of dust devils and clouds on Mars, Proc. IEEE Int. Conf. Image Proc. (Atlanta 2006) pp. 2765–2768
- 45.40 L. Matthies: Stereo vision for planetary rovers: stochastic modeling to near real-time implementation, Int. J. Comp. Vision **8**(1), 71–91 (1992)
- 45.41 K. Yoshida, D.N. Nenchev, M. Uchiyama: Moving base robotics and reaction management control, Robot. Res.: 7th Int. Symp., ed. by G. Giralt, G. Hirzinger (Springer, New York 1996) pp. 101–109
- 45.42 J. Russakow, S.M. Rock, O. Khatib: An operational space formulation for a free-flying multi-arm space robot, 4th Int. Symp. Exp. Robot. (1995) pp. 448–457
- 45.43 Y. Umetani, K. Yoshida: Continuous path control of space manipulators mounted on OMV, Acta Astro. **15**(12), 981–986 (1987), presented at the 37th IAF Conf, Oct. 1986
- 45.44 Y. Umetani, K. Yoshida: Resolved motion rate control of space manipulators with generalized jacobian matrix, IEEE Trans. Robot. Autom. **5**(3), 303–314 (1989)
- 45.45 Y. Xu, T. Kanade (eds.): *Space Robotics: Dynamics and Control* (Kluwer Academic, Boston 1993)
- 45.46 K. Yoshida: Impact dynamics representation and control with extended inversed inertia tensor for space manipulators, Robot. Res. 6th Int. Symp., ed. by T. Kanade, R. Paul (1994) pp. 453–463
- 45.47 K. Yoshida: Experimental study on the dynamics and control of a space robot with the experimental free-floating robot satellite (EFFORTS) simulators, Adv. Robot. **9**(6), 583–602 (1995)
- 45.48 Y. Nakamura, R. Mukherjee: Nonholonomic path planning of space robots via a bidirectional approach, IEEE Trans. Robot. Autom. **7**(4), 500–514 (1991)
- 45.49 S. Dubowsky, M. Torres: Minimizing attitude control fuel in space manipulator systems, Proc. Int. Symp. AI Robot. Autom. (i-SAIRAS) (1990) pp. 259–262
- 45.50 S. Dubowsky, M. Torres: Path planning for space manipulators to minimize spacecraft attitude disturbances, Proc. IEEE Int. Conf. Robot. Autom., Vol. 3 (Sacramento 1991) pp. 2522–2528
- 45.51 K. Yoshida: Practical coordination control between satellite attitude and manipulator reaction dynamics based on computed momentum concept, Proc. 1994 IEEE/RSJ Int. Conf. Intell. Robot. Syst. (Munich 1994) pp. 1578–1585
- 45.52 M. Oda: Coordinated control of spacecraft attitude and its manipulator, Proc. 1996 IEEE Int. Conf. Robot. Autom. (1996) pp. 732–738
- 45.53 Z. Vafa, S. Dubowsky: On the dynamics of manipulators in space using the virtual manipulator approach, Proc. IEEE Int. Conf. Robot. Autom. (1987) pp. 579–585
- 45.54 E. Papadopoulos, S. Dubowsky: Dynamic singularities in the control of free-floating space manipulators, ASME J. Dyn. Syst. Meas. Contr. **115**(1), 44–52 (1993)
- 45.55 Y. Umetani, K. Yoshida: Workspace and manipulability analysis of space manipulator, Trans. Soc. Instrum. Contr. Eng. **E-1**(1), 116–123 (2001)
- 45.56 D.N. Nenchev, Y. Umetani, K. Yoshida: Analysis of a redundant free-flying spacecraft/manipulator system, IEEE Trans. Robot. Autom. **8**(1), 1–6 (1992)
- 45.57 D.N. Nenchev, K. Yoshida, P. Vichitkulsawat, M. Uchiyama: Reaction null-space control of flexible structure mounted manipulator systems, IEEE Trans. Robot. Autom. **15**(6), 1011–1023 (1999)
- 45.58 D.N. Nenchev, K. Yoshida, M. Uchiyama: Reaction null-space based control of flexible structure mounted manipulator systems, Proc. IEEE 35th CDC (1996) pp. 4118–4123
- 45.59 W.J. Book, S.H. Lee: Vibration control of a large flexible manipulator by a small robotic arm, Proc. Am. Contr. Conf. (Pittsburgh 1989)
- 45.60 M.A. Torres: Modelling, path-planning and control of space manipulators: the coupling map concept. Ph.D. Thesis (MIT, Cambridge 1993)
- 45.61 S. Abiko, K. Yoshida: An effective control strategy of japanese experimental module remote manipulator system (JEMRMS) using coupled and un-coupled dynamics, Proc. 7th Int. Symp. Artif. Intell. Robot. Autom. Space Paper AS18 (CD-ROM) (Nara 2003)
- 45.62 S. Abiko: Dynamics and Control for a Macro-Micro Manipulator System Mounted on the International Space Station. Ph.D. Thesis (Tohoku University, Sendai 2005)
- 45.63 S. Abiko, K. Yoshida: On-line parameter identification of a payload handled by flexible based manipulator, Proc. IEEE/RSJ Int. Conf. Intell. Robot. Syst. (IROS'04) (Sendai 2004) pp. 2930–2935
- 45.64 S. Abiko, K. Yoshida: An adaptive control of a space manipulator for vibration suppression, Proc. IEEE/RSJ Int. Conf. Intell. Robot. Syst. (IROS'05) (Edmonton 2005)
- 45.65 G. Gilardi, I. Shraf: Literature survey of contact dynamics modeling, Mech. Machine Theory **37**, 1213–1239 (2002)
- 45.66 K. Yoshida, H. Nakanishi, H. Ueno, N. Inaba, T. Nishimaki, M. Oda: Dynamics, control, and impedance matching for robotic capture of a non-cooperative satellite, Adv. Robot. **18**(2), 175–198 (2004)
- 45.67 H. Nakanishi, K. Yoshida: Impedance control of free-flying space robot for orbital servicing, J. Robot. Mechatron. **18**(5), 608–617 (2006)
- 45.68 P.M. Pathak, A. Mukherjee, A. DasGupta: Impedance control of space robots using passive degrees of freedom in controller domain, J. Dyn. Syst. Meas. Contr. **127**, 564–578 (2006)

- 45.69 S. Abiko, R. Lampariello, G. Hirzinger: Impedance control for a free-floating robot in the grasping of a tumbling target with parameter uncertainty, IEEE/RSJ Int. Conf. Intell. Robot. Syst. (IROS '06) (Beijing 2006)
- 45.70 K. Iagnemma, H. Shibly, S. Dubowsky: On-Line traction parameter estimation for planetary rovers, Proc. IEEE Int. Conf. Robot. Autom. (ICRA '02) (Washington 2002)
- 45.71 K. Yoshida, H. Hamano: Motion dynamics of a rover with slip-based traction model, Proc. IEEE Int. Conf. Robot. Autom. (ICRA '02) (Washington 2002)
- 45.72 A. Jain, J. Guineau, C. Lim, W. Lincoln, M. Pomerantz, G. Sohl, R. Steele: Roams: planetary surface rover simulation environment, Proc. 7th Int. Symp. Artif. Intell. Robot. Autom. Space (ISAIRAS '03) (Nara 2003)
- 45.73 K. Yoshida, G. Ishigami: Steering characteristics of a rigid wheel for exploration on loose soil, Proc. IEEE Int. Conf. Intell. Robot. Syst. (IROS '04) (Sendai 2004)
- 45.74 R. Bauer, W. Leung, T. Barfoot: Experimental and simulation results of wheel-soil interaction for planetary rovers, Proc. IEEE Int. Conf. Intell. Robot. Syst. (IROS '05) (Edmonton 2005)
- 45.75 G. Ishigami, K. Yoshida: Steering characteristics of an exploration rover on loose soil based on all-wheel dynamics model, Proc. IEEE Int. Conf. Intell. Robot. Syst. (IROS '05) (Edmonton 2005)
- 45.76 A. Ellery, N. Patel, R. Bertrand, J. Dalcomo: Exomars rover chassis analysis and design, Proc. 8th Int. Symp. Artif. Intell. Robot. Autom. Space (ISAIRAS '05) (Munich 2005)
- 45.77 A. Gibbesch, B. Schäfer: Multibody system modelling and simulation of planetary rover mobility on soft terrain, Proc. 8th Int. Symp. Artif. Intell. Robot. Autom. Space (ISAIRAS '05) (Munich 2005)
- 45.78 G. Ishigami, A. Miwa, K. Nagatani, K. Yoshida: Terramechanics-based model for steering maneuver of planetary exploration rovers on loose soil, J. Field Robot. **24**(3), 233–250 (2007)
- 45.79 J.Y. Wong: *Theory of Ground Vehicles* (Wiley, New York 1978)
- 45.80 K. Iagnemma, S. Dubowsky: *Mobile Robots in Rough Terrain: Estimation, Motion Planning, and Control With Application to Planetary Rovers*, Springer Tracts in Advanced Robotics, Vol. 12 (Springer, Berlin, Heidelberg 2004)
- 45.81 K. Yoshida, T. Watanabe, N. Mizuno, G. Ishigami: Terramechanics-based analysis and traction control of a lunar/planetary rover, Proc. Int. Conf. Field Service Robot. (FSR '03) (Yamanashi 2003)
- 45.82 J.Y. Wong, A.R. Reece: Prediction of rigid wheel performance based on the analysis of soil-wheel stresses. Part I, performance of driven rigid wheels, J. Terramechan. **4**, 81–98 (1967)
- 45.83 Z. Janosi, B. Hanamoto: The analytical determination of drawbar pull as a function of slip for tracked vehicle in deformable soils, Proc 1st Int. Conf. Terrain-Vehicle Syst. (Torino 1961)
- 45.84 E. Hegedus: A simplified method for the determination of bulldozing resistance, Land Locomotion Research Laboratory, Army Tank Automotive Command Report, Vol. 61, 1960
- 45.85 I. Rekleitis, E. Martin, G. Rouleau, R. L'Archeveque, K. Parsa, E. Dupuis: Autonomous capture of a tumbling satellite, J. Field Robot. **24**(4), 275–296 (2007)
- 45.86 R. Ambrose: <http://robonaut.jsc.nasa.gov/> Jan (2008)
- 45.87 J. Blamont: Balloons on other planets, Adv. Space Res. **1**, 63–69 (1981)
- 45.88 J.A. Cutts, K.T. Nock, J.A. Jones, G. Rodriguez, J. Balaram, G.E. Powell, S.P. Synott: Aerovehicles for planetary exploration, IEEE Int. Conf. Robot. Autom. (Nagoya 1995)
- 45.89 M.K. Heun, J.A. Jones, J.L. Hall: Gondola design for Venus deep-atmosphere aerobot operations, AIAA, 36th Aerospace Sci. Meeting Exhibit, 1998 ASME Wind Energy Symp. (Reno 1998)
- 45.90 S. Miller, J. Essmiller, D. Beaty: Mars deep drill – a mission concept for the next decade, Space Conf. Exhibit (San Diego 2004) pp. 2004–6048, AIAA
- 45.91 S. Mukherjee, P. Bartlett, B. Glass, J. Guerrero, S. Stanley: Technologies for exploring the martian subsurface, IEEE Aerospace Conf. Proc. (Big Sky 2006), No. 1349
- 45.92 S.B. Skaar: Teleoperation and robotics in space. In: *Progress in Astronautics and Aeronautics Series*, ed. by C.F. Ruoff (AIAA Technology and Industrial Arts, Notre Dame 1994), ISBN 1563470950
- 45.93 G. F. Bekey: Assessment of international research and development in robotics a study report of the national science foundation/NASA study, available at <http://www.wtec.org/robotics/> (soon to be published in book form from World Scientific Publishing in Singapore).
- 45.94 Assessment of Options for Extending the Life of the Hubble Space Telescope, National Research Council: Final Report, (National Academies Press, 2005) ISBN-10: 0-309-09530-1, ISBN-13: 978-0-309-09530-3
- 45.95 A.M. Howard, E.W. Tunstel: *Intelligence for Space Robotics* (TSI Press, San Antonio 2006), ISBN 1-889335-26-6/1-889335-29-0.
- 45.96 T.B. Sheridan: Space teleoperation through time delay: review and prognosis, IEEE Trans. Robot. Autom. **9**(5), 592–606 (1993)
- 45.97 J. Field Robot. Special Issue on Space Robotics, Part I–Part III, **24**(3–5), 167–434 (2007)